ISOTHERMAL GAS-LIQUID FLOW

USING THE LATTICE BOLTZMANN METHOD

A Thesis

by

DONGHOON KIM

Submitted to the Office of Graduate Studies of
Texas A&M University
in partial fulfillment of the requirements for the degree of

MASTER OF SCIENCE

August 2011

Major Subject: Nuclear Engineering

ISOTHERMAL GAS-LIQUID FLOW

USING THE LATTICE BOLTZMANN METHOD

A Thesis

by

DONGHOON KIM

Submitted to the Office of Graduate Studies of
Texas A&M University
in partial fulfillment of the requirements for the degree of

MASTER OF SCIENCE

Approved by:

Chair of Committee,	Yassin A. Hassan
Committee Members,	William H. Marlow
	Kalyan Annamalai
Head of Department,	Raymond J. Juzaitis

August 2011

Major Subject: Nuclear Engineering

ABSTRACT

Isothermal Gas-liquid Flow Using the Lattice Boltzmann Method. (August 2011)

Donghoon Kim, B.S., Republic of Korea Naval Academy

Chair of Advisory Committee: Dr. Yassin A. Hassan

As the operating conditions of the pressurized water reactor (PWR) have been increased towards the thermal limits of the core for economics, the subcooled boiling heat transfer performance of the rod bundles under normal operating conditions has become an increasingly important design focus. Effective field models such as two-fluid model, on which most previous numerical studies in the nuclear fields have focused, cannot predict detailed phenomenon of subcooled boiling because it involves complex multiphase dynamics, such as nucleation, growth, detachment bubbles from a wall, deformation, break-up, coalescence, and condensation. It also requires numerous, additional closure relations. On the other hand, direct numerical simulations with interfacial tracking enable us to capture specific two-phase flow and do not require additional empirical closure relations.

This thesis simulates isothermal two-dimensional bubble dynamics as a starting point toward direct simulation of the subcooled boiling by adopting a lattice Boltzmann method with the phase-field model. The lattice Boltzmann method is a mesoscopic approach well-adapted to the simulation of complex fluids and is simple to implement.

The phase field model can capture complex topological deformation, such as

coalescence and break-up, with better numerical stability than other interfacial tracking methods like Volume of Fluid (VOF) and level set methods.

We validate the present method for stationary and moving two-phase interfaces by comparing with theoretical solutions for a single static bubble in a stationary liquid and a capillary wave, respectively. In addition, the capability of the current method to simulate the coalescence of two bubbles and droplets is validated by comparing with experimental data.

To see the applicability of the method to problems involving complex bubble behaviors and interactions with a high-density ratio as in subcooled boiling water, we simulate rising single and double bubbles in a viscous fluid. For a single bubble problem, the bubble shapes and terminal velocity agreed well with the experimental results for different fluid dynamic conditions. For a double bubble case, the current method can capture the interaction and dynamics of the bubbles. Thus, it is expected that this study can serve as a stepping-stone extension to convective subcooled boiling heat transfer in the nuclear reactor core.

DEDICATION

To my wife Guinam and our children Junseok and Do-heon.

ACKNOWLEDGEMENTS

I would like to thank my committee chair, Dr. Yassin A. Hassan, and my committee members, Dr. William H. Marlow and Dr. Annamalai Kalyan. Thanks also go to my friends and colleagues, and the department faculty and staff, for making my time at Texas A&M University a great experience.

I also want to extend my gratitude to the Republic of Korea Navy, which supported my study for two years, and to all of the friends and Korean students in the nuclear engineering department.

Especially, I would also like to thank Dr. Shin kyu Kang for his guidance and support throughout the course of this research.

Finally, I would like to thank my family. Thanks to my parents for their encouragement and endless love, and to my sisters for their care and help. And most of all, special thanks to my wife Guinam and our children Junseok and Do-heon for their sacrifice, understanding, patience, encouragement, and love. I am forever grateful.

TABLE OF CONTENTS

LIST OF FIGURES

Page

Page

Page

Page

LIST OF TABLES

CHAPTER I

INTRODUCTION

Background

In recent years, due to pressures to improve the economics of power generation and plant performance, plant up-ratings, higher fuel burn-up, longer fuel cycles, and higher enrichment have been conducted in pressurized water reactor (PWR), thus increasing local subcooled boiling in the core region under normal operating conditions. Hence, the accurate prediction and understanding of the subcooled boiling has become a significant issue in the nuclear field.

However, subcooled boiling is difficult to predict because it involves complex physics, such as nucleation, growth, detachment of individual bubbles from a wall, bubble deformation, bubble break-up, coalescence, and condensation. In most previous studies in nuclear engineering, effective field methods, such as the two-fluid model in which statistically, temporally, or spatially averaged equations are used for two-phase flow simulation, have been practically used. But the two-fluid model basically requires closure relations for the phase-to-phase momentum and heat transfers and bubble population. The closure relations have traditionally been determined through a combination of dimensional arguments and correlation of experimental data. In particular, simple semi-empirical models for bubble drag, condensation, breakup, and coalescence are used under the assumption of idealized geometries for the vapor-liquid

---

This thesis follows the style of *International Journal for Numerical Methods in Fluids.*

interface, that is, spherical, elliptical, or symmetric bubbles. However, the geometry of the liquid-vapor interface is very irregular and shows dynamic behaviors.

In contrast, direct numerical simulations (DNS) with interfacial tracking do not require the empirical closure correlations. Instead, the unsteady Navier–Stokes equations are solved on fine grids to resolve all flow scales fully. Several DNS interface-capturing methods, such as the volume of fluid (VOF) method [1], the front-tracking technique [2], and level set method [3], have been developed. These conventional approaches may have numerical difficulties in the treatment of topological deformation of interfacial break and coalescence. This is because in most multiphase fluid systems of interest, discontinuity occurs in the system due to the abrupt change of physical properties such as density and viscosity across the interface.

In the phase field model (PFM), an interface is described as a finite volumetric zone across which the physical properties (mass density, concentration, and viscosity) vary steeply and continuously. The shape of the interface is determined to minimize the free energy of the system [4-5]. Therefore, in PFM-based numerical simulations, the boundary condition of phase is not required for the interface. Unlike conventional interface-tracking methods, surface tension in the PFM is given as surface free energy per unit area caused by a local density gradient. The PFM reconstructs the interface autonomously by considering a chemical potential gradient. Therefore, the effect of the surface tension force on the flow fields can be treated without complex topological calculation of the interfacial profile. As a result, the PFM-based method can easily

reproduce interfacial displacement due to phase changes or dissolution [6]. It also can simulate complex two-phase flows more efficiently than other methods can.

On the other hand, due to its simplicity and efficiency, the lattice Boltzmann method (LBM) has been broadly used to simulate incompressible viscous flows as an alternative to the Navier–Stokes methods [7-8]. The lattice Boltzmann equation (LBE) is a kinetic equation of particle density distribution functions (PDDF) discretized on the Cartesian grid. The LBM is especially well-adapted to the simulation of complex fluids because the method very naturally takes charge of the relevant physical ingredients.

Multiphase LBMs commonly adopted can be categorized into four different types: color-gradient model, Shan-Chen model, He et al.'s model, and the free energy model.

The color-gradient model [9] proposed by Gunstensen et al. is based on the Rothman-Keller (R-K) lattice gas model [10] in which the surface tension, the ratios of densities, and viscosities can be independently adjusted [11].

The Shan-Chen (S-C) model [12] was developed to simulate multiphase fluids with high-density ratios [13]. However, this model cannot independently adjust the surface tension and the ratios of densities and viscosities. Besides, some parameters need to be determined through additional numerical experiments [11]. Pan et al. [14] and Li et al. [15] applied the S-C model to investigate the two-component flow in porous media. However, due to the numerical instability, the maximum viscosity ratio was about 3 [15].

In He et al.'s model [16], two sets of PDDFs and the concept of the index function were adopted to reduce the numerical instability caused by large intermolecular forces along the interface. However, the mobility related to the density could not be chosen

flexibly. Lee and Lin [17] developed an LBM for multiphase-flows with large density ratio based on He et al.'s model [16]. However, since the discretization forms are changed at different steps in Lee and Lin's model, the implementation was quite complex. The color-gradient, S-C, and He et al.'s models did not explicitly describe the evolution of the interface and the physics of the interface capturing equation was not clear.

On the other hand, based on a free energy functional, Swift et al. [18] proposed the free energy (FE) LBM. The FE LBM can be regarded as the PFM because it constructed the discrete kinetic equation equivalent to the evolution equation of order parameter using s free energy approach. In contrast with the S-C model, local momentum conservation was preserved. However, this model could not satisfy the Galilean invariance except for the binary ideal fluids [18-19]. Inamuro et al. [20] simulated a high-density ratio through improving Swift et al.'s free energy model. However, this model has to solve a Poisson equation, which demands more computational time until convergence. In this model, the pressure correction is applied to enforce the continuity condition after every collision-streaming step, which is similar to the VOF method and level set method. The projection step would reduce the efficiency of the method greatly. A small drawback is that the cut-off value of the order parameter and the surface tension coefficient are not given analytically. It is also found that the model may not be accurate for some incompressible flows although the projection procedure is employed to secure the incompressible condition. Recently, Zheng et al. proposed a Galilean invariant FE LBM [21]. This model can recover the Cahn-Hilliard equation without any additional

terms, thus keeping the Galilean invariance property. In addition, this model could simulate two-phase fluids with high-density ratios without adopting any additional numerical treatment as in Inamuro et al.

Objective

The objective of this study is to simulate isothermal, two-phase flows with a large density ratio directly using the phase-field model under the LBM frame as a starting point for simulating convective subcooled boiling heat transfer in PWRs. We focus on the bubble topologies, including the coalescence and its dynamics under different non-dimensional numbers, such as the Eötvös number (Eo), and the Morton number (M).

CHAPTER II

NUMERICAL METHODOLOGY

This chapter explains the numerical methodology of LBM with phase field modeling. In the phase field modeling, the Navier-Stokes equations (NSE) and the Cahn-Hilliard equation (CHE) can describe the fluid and interface [22-24]:

$$\frac{\partial n}{\partial t} + \nabla \cdot \left(n\mathbf{u} \right) = 0, \tag{1}$$

$$\frac{\partial \left(n\mathbf{u} \right)}{\partial t} + \nabla \cdot \left(n\mathbf{uu} \right) = -\nabla \cdot \mathbf{P} + \mu \nabla^2 \mathbf{u} + \mathbf{F}_b, \tag{2}$$

$$\frac{\partial \phi}{\partial t} + \nabla \cdot \left(\phi \mathbf{u} \right) = \theta_M \nabla^2 \mu_\phi, \tag{3}$$

where t is the time; $\mathbf{u}$ is the macroscopic velocity; $\mathbf{P}$ is the pressure tensor; μ is the dynamic viscosity; $\mathbf{F}_b$ is the body force; θ_M is the mobility; μ_Φ is the chemical potential; n is the average number density defined by

$$n = \frac{\rho_A + \rho_B}{2}, \tag{4}$$

and ϕ is the expected order parameter or phase field that tracks the interface defined by

$$\phi = \frac{\rho_A - \rho_B}{2} \tag{5}$$

in which ρ_A and ρ_B are the density of fluids A and B. In order to describe the thermodynamic behavior from the mean-field theory, we adopt a free energy functional of the form [21-22] defined by

$$F = \int f\left(n,\phi,\nabla\phi\right)dV = \int\left[\psi\left(\phi\right)+\frac{\kappa}{2}\left|\nabla\phi\right|^2 + nRT\ln\left(n\right)\right]dV \tag{6}$$

where V is a control volume; ψ is the bulk free energy density per unit mass for the homogenous system; κ is a coefficient associated with the surface tension and the thickness of the interface region by

$$\kappa = \frac{3\sigma W}{8\phi^{*2}} \tag{7}$$

in which W is the interface width; R is the gas constant; and T is the temperature. In this study, the bulk free energy density is chosen as a double-well form [21-22] defined by

$$\psi\left(\phi\right) = a\left(\phi^2 - \phi^{*2}\right)^2, \tag{8}$$

in which ϕ^* is a constant from the bulk free energy equilibrium state, $\phi = \pm\phi^*$, defined by

$$\phi^* = \frac{\rho_A - \rho_B}{2} \tag{9}$$

a is an amplitude parameter to control the two-phase interaction and is related to

$$a = \frac{3\sigma}{4W\phi^{*4}}, \tag{10}$$

and the chemical potential is computed by

$$\mu_\phi = \frac{\partial f\left(n,\phi,\nabla\phi\right)}{\partial\phi} - \nabla\cdot\frac{\partial f\left(n,\phi,\nabla\phi\right)}{\partial\nabla\phi} = 4a\phi\left(\phi^2 - \phi^{*2}\right) - \kappa\nabla^2\phi. \tag{11}$$

In Equation (2), the term $-\nabla\cdot\mathbf{P}$ is related to the surface tension force. This force can be rewritten as a potential term [23, 25]:

$$\mathbf{F}_s = -\nabla \cdot \mathbf{P} = -\phi \nabla \mu_\phi - \nabla p_0, \tag{12}$$

where $p_0 = nc_s^2$.

The hydrodynamic equations

In terms of the two-phase LBM, Equations (1), and (2) without a forcing term can be expressed as [26-27]:

$$f_\alpha\left(\mathbf{x}+\mathbf{e}_\alpha \Delta t, t+\Delta t\right) = f_\alpha\left(\mathbf{x},t\right) - \frac{1}{\tau_n}\left[f_\alpha\left(\mathbf{x},t\right) - f_\alpha^{(\mathrm{eq})}\left(\mathbf{x},t\right)\right], \tag{13}$$

where f_α is the distribution function for the hydrodynamic field at position $\mathbf{x}$ and time t for the discrete velocity; $\mathbf{e}_\alpha$ is the αth direction; and τ_n is the dimensionless single relaxation parameter related to the fluid viscosity due to fluid-particle collisions. The equilibrium particle density distribution function, $f_\alpha^{(\mathrm{eq})}$ is given by [28]

$$f_\alpha^{(\mathrm{eq})} = w_\alpha \left\{ A_\alpha + n\left[\frac{\mathbf{e}_\alpha \cdot \mathbf{u}}{c_s^2} + \frac{\left(\mathbf{e}_\alpha \cdot \mathbf{u}\right)^2}{2c_s^4} - \frac{\mathbf{u}^2}{2c_s^2} \right] \right\}, \tag{14}$$

with the coefficient A_α given by

$$A_\alpha = \begin{cases} \dfrac{\left(nc_s^2 + \phi\mu_\phi\right)}{c_s^2} = A, & \alpha = 1,2,3,4,5,6,7,8, \\ w_\alpha^{-1}\left[n - \left(1-w_\alpha\right) A \right], & \alpha = 0, \end{cases} \tag{15}$$

where c_s is the sound speed related to the unit lattice cell speed as

$$c = \sqrt{3} c_s, \tag{16}$$

in which the lattice speed $c = \Delta x / \Delta t$, and Δx and Δt are the lattice size and the time step size, respectively. The weighting coefficient, w_α, depends on the discrete velocity set,

$\{\mathbf{e}_\alpha\}$. The nine-velocity LBE model on a square lattice, called the D2Q9 model, has been widely used for two-dimensional flow simulations [29-30]. In the D2Q9 model, discrete velocity vectors (Figure 1) are defined by

$$\mathbf{e}_\alpha = \begin{cases} (0,0), & \alpha = 0, \\ c(\cos\theta, \sin\theta), & \theta = \dfrac{\pi}{2}(\alpha - 1), \quad \alpha = 1,2,3,4, \\ \sqrt{2}c(\cos\theta, \sin\theta), & \theta = \dfrac{\pi}{2}(\alpha - 5) + \dfrac{\pi}{4}, \quad \alpha = 5,6,7,8. \end{cases} \tag{17}$$

and the corresponding weighting coefficients, w_α, are

$$w_a = \begin{cases} \dfrac{4}{9}, & \alpha = 0, \\ \dfrac{1}{9}, & \alpha = 1,2,3,4, \\ \dfrac{1}{36}, & \alpha = 5,6,7,8. \end{cases} \tag{18}$$

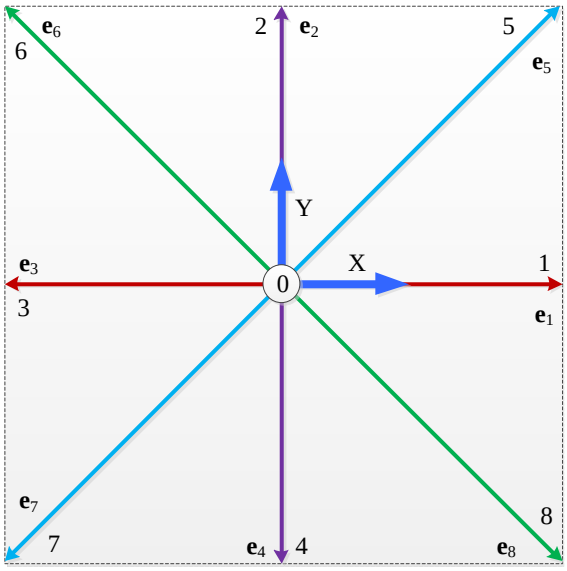

Figure 1. The discrete velocity vectors directions in the D2Q9 model.

Density and velocity can be computed by taking the zeroth and first moments of the particle density distribution functions, respectively,

$$n = \sum_{\alpha} f_{\alpha} = \sum_{\alpha} f_{\alpha}^{(\mathrm{eq})} , \tag{19}$$

$$n\mathbf{u} = \sum_{\alpha} \mathbf{e}_{\alpha} f_{\alpha} = \sum_{\alpha} \mathbf{e}_{\alpha} f_{\alpha}^{(\mathrm{eq})} , \tag{20}$$

When an external force exists, the lumped-forcing LBE can be described in the following explicit form [26-27],

$$f_{\alpha}\left(\mathbf{x}+\mathbf{e}_{\alpha}\Delta t, t+\Delta t\right) = f_{\alpha}\left(\mathbf{x},t\right) - \frac{1}{\tau_n}\left[f_{\alpha}\left(\mathbf{x},t\right) - f_{\alpha}^{(\mathrm{eq})}\left(\mathbf{x},t\right)\right] + F_{\alpha}\left(\mathbf{x},t\right)\Delta t . \tag{21}$$

The split-forcing LBE is adopted, which enables it to recover the NSE (continuity and momentum equations) with second-order accuracy even for an unsteady, non-uniform force [31]. They inserted the external force effect to the momentum by redefining the velocity as

$$n\mathbf{u} = \sum_{\alpha} \mathbf{e}_{\alpha} f_{\alpha} + \frac{\Delta t}{2}\mathbf{F} , \tag{22}$$

Hence, the discrete force distribution function can be defined as

$$F_{\alpha}\left(\mathbf{x},t\right) = \left(1-\frac{1}{2\tau_n}\right) w_{\alpha}\left[3\frac{\mathbf{e}_{\alpha}-\mathbf{u}\left(\mathbf{x},t\right)}{c^2} + 9\frac{\mathbf{e}_{\alpha}\cdot\mathbf{u}\left(\mathbf{x},t\right)}{c^4}\mathbf{e}_{\alpha}\right]\cdot\mathbf{F}\left(\mathbf{x},t\right) \tag{23}$$

which satisfies the following relations of the zeroth and the first moments

$$\sum_{\alpha} F_{\alpha}\left(\mathbf{x},t\right) = 0 , \tag{24}$$

$$\sum_{\alpha} \mathbf{e}_{\alpha} F_{\alpha}\left(\mathbf{x},t\right) = \left(1-\frac{1}{2\tau_n}\right)\mathbf{F}\left(\mathbf{x},t\right) . \tag{25}$$

The interface-capturing equation

In terms of the two-phase LBM, Equation (3) for the interface-capturing can be written as [26-27]

$$g_\alpha\left(\mathbf{x}+\mathbf{e}_\alpha\Delta t, t+\Delta t\right)=g_\alpha\left(\mathbf{x},t\right)-\frac{1}{\tau_\phi}\left[g_\alpha\left(\mathbf{x},t\right)-g_\alpha^{(\mathrm{eq})}\left(\mathbf{x},t\right)\right], \tag{26}$$

where g_α is the distribution function for the concentration field (ϕ); and τ_ϕ is the dimensionless single relaxation parameter related to the mobility. The chemical potential can be included in the LBE through the equilibrium distribution function given by [28]

$$g_\alpha^{(\mathrm{eq})}=w_\alpha\left[B_\alpha+\frac{\phi\left(\mathbf{e}_\alpha\cdot\mathbf{u}\right)}{c_s^2}\right], \tag{27}$$

with the coefficient B_α given by

$$B_\alpha=\begin{cases}\dfrac{\Gamma\mu_\phi}{c_s^2}=B, & \alpha=1,2,3,4,5,6,7,8,\\ w_\alpha^{-1}\left[n-\left(1-w_\alpha\right)B\right], & \alpha=0,\end{cases} \tag{28}$$

where Γ is used to control the mobility.

The order parameter can be computed after the streaming step by

$$\phi=\sum_\alpha g_\alpha=\sum_\alpha g_\alpha^{(\mathrm{eq})}. \tag{29}$$

For validation of the present method, we start with static bubble and then consider a capillary wave with a moving interface between two phases. In addition, we test the capability of the current method to simulate coalescence of two bubbles. Next, we apply the method to the problem of an up-rising bubble with a large density ratio.

CHAPTER III

RESULTS AND DISCUSSION

A bubble in the stationary liquid

For the LBM with phase-field modeling, it is necessary to verify the effect of the static and moving interface layer in the phase field. To study the static case, the fundamental test is a two-dimensional single circular bubble surrounded by stationary liquid in the domain with no gravity force.

The pressure difference between the inside and outside of the bubble is calculated by the LBM with phase-field modeling. The calculation results are compared with the theoretical solution to verify the suitability of the LBM. A circular bubble is located at the center of the two-dimensional domain. The density ratio is set to be 1000 to simulate a high-density ratio.

According to Laplace law, the pressure difference between the inside and outside of a two-dimensional bubble at equilibrium is related to the surface tension by

$$\Delta p = p_{in} - p_{out} = \frac{\sigma}{R}, \tag{30}$$

where Δp is the pressure difference across the interface; and R is the bubble radius. The pressure p in the free-energy model is related to the pressure tensor defined by [7, 18, 32]

$$\mathbf{P}_{ij} = p\delta_{ij} - \kappa\left[\left(\nabla\phi\right)^2 \delta_{ij} - \nabla_i\phi\nabla_j\phi\right]. \tag{31}$$

The numerical result for the pressure can be calculated by

$$p = a\left(3\phi^4 - 2\phi^{*2}\phi^2 - \phi^{*4}\right) - \kappa\phi\nabla^2\phi - \frac{\kappa}{2}\left(\nabla\phi\right)^2 + nRT \,. \tag{32}$$

To eliminate errors induced by the interfacial layer width, the pressure difference is calculated by averaging the pressures inside and outside the bubble at a lattice point away from $R \pm W$.

To evaluate the bubble radius (R) during the calculation, we adopt the effective bubble diameter (for a two-dimensional bubble in simulations), which is defined by

$$D_e = \sqrt{\frac{4A}{\pi}}\,, \tag{33}$$

where A is the area of the bubble ($\phi < 0$).

In this calculation, we adopt the following convergence criterion

$$\max\left(\sqrt{u_{n+1}^2 + v_{n+1}^2} - \sqrt{u_n^2 + v_n^2}\right) < 10^{-12}\,, \tag{34}$$

in which u and v are the velocity components in the x and y directions, respectively.

A circular bubble with radius (R) is located at the center of the domain. The mesh size is taken as $5R \times 5R$. The periodic boundary condition is adopted at all boundaries. The densities are set to be $\rho_H = 1000$, and $\rho_L = 1$. The mobility coefficient (Γ) is chosen as 100. The single relaxation time is set as $\tau_n = 0.875$ and $\tau_\phi = 0.7$. The parameter W, which can govern the numerical interfacial thickness, is set to 5. We adopt the order parameter profile along the direction normal to a bubble interface z by [22]

$$\phi = \pm\phi^* \tanh\left(\frac{2z}{W}\right), \tag{35}$$

where z is the position of the interfacial layer. The initial order parameter $\pm\phi^*$ is set to be ±499.5, which corresponds to the density difference.

To investigate the pressure variations with different radii and the surface tensions, we take the surface tension coefficients (σ) as 0.1, 0.2, and 0.3, respectively. The radii (R) are set to 10, 20, 30, 40, 50, and 60.

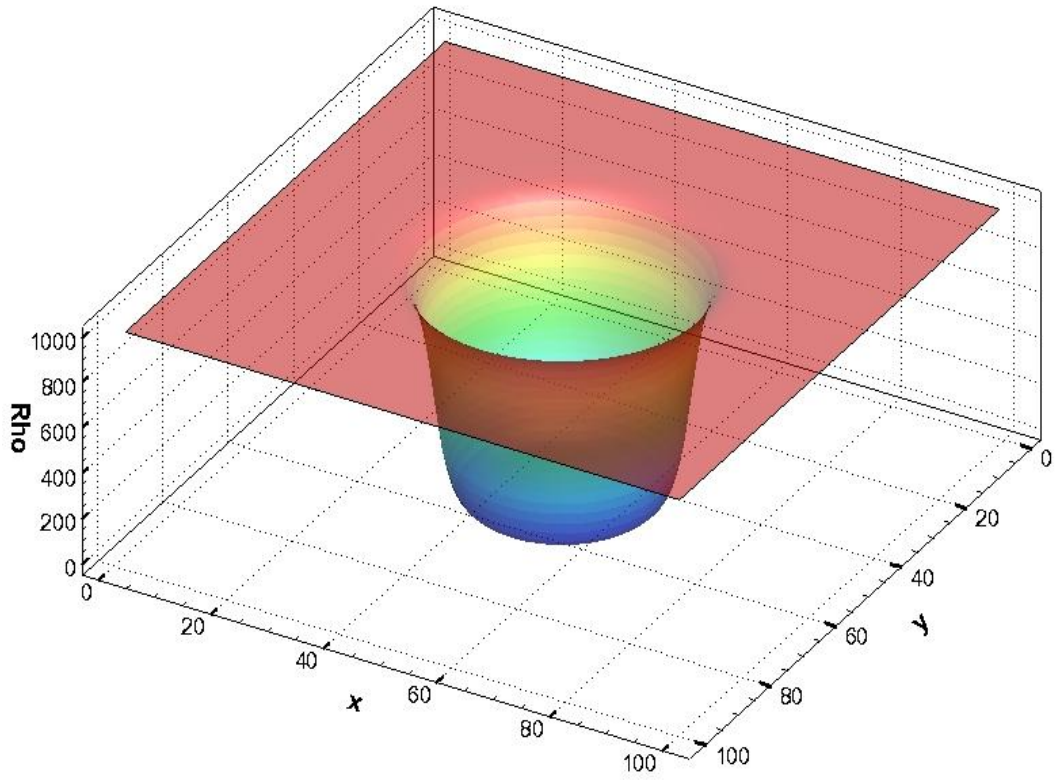

Figure 2. The density profile between the two-phase fluids at steady-state.

Figure 2 describes the density difference between the two-phase fluids at steady-state. The density of the bubble inside and outside are generated in the same way as the initial condition ($\rho_H = 1000$, $\rho_L = 1$), respectively. In the interfacial region, the density is smoothly changed to prevent an abrupt shift by the interfacial layer thickness parameter (W).

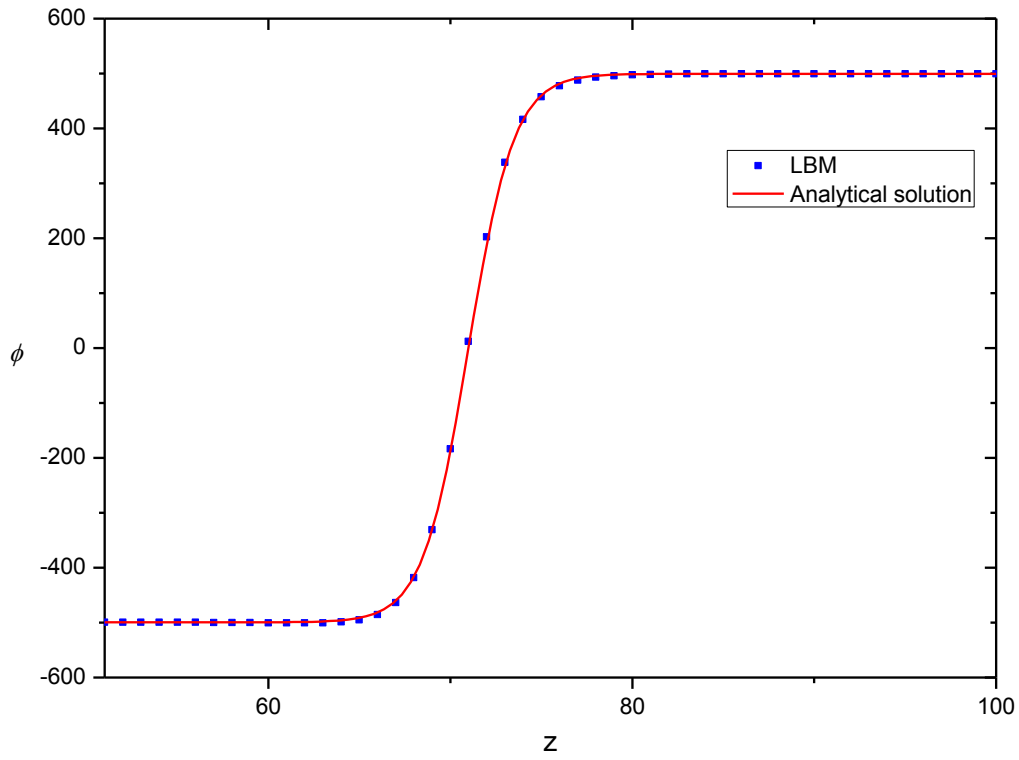

Figure 3. The order parameter (ϕ) profile along the interface of the bubble.

Figure 3 displays the order parameter at all the lattice points as a function of the distance from the center of the bubble. All data points from the simulation agree well with the analytical curve as calculated from Equation (35).

Due to finite lattice directions and the isotropic derivatives in the LBM, spurious currents can be generated in the simulation of two-phase system and the eight symmetric eddies with very small magnitude velocity (10^{-8}) are formed, as shown in Figure 4.

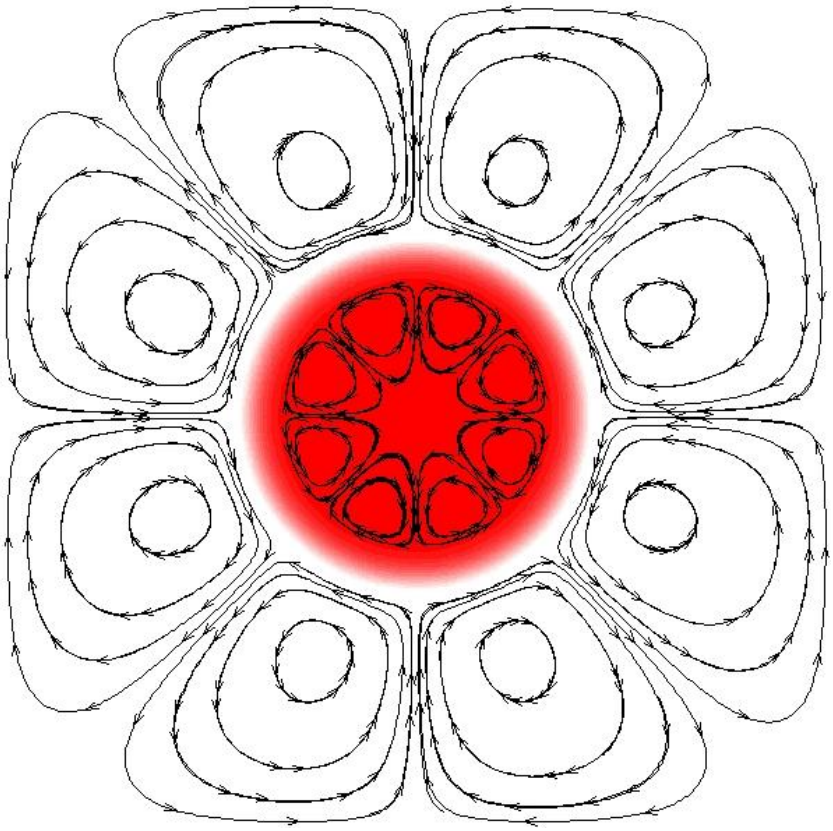

Figure 4. Streamline of spurious currents around the single bubble.

Figure 5 shows the time variation of the maximum spurious velocity in the domain. It is seen that the maximum velocity decreases by an order of 10^{-8}, and that the magnitude of currents are smaller than the Lee-Fischer LB model (10^{-5}).

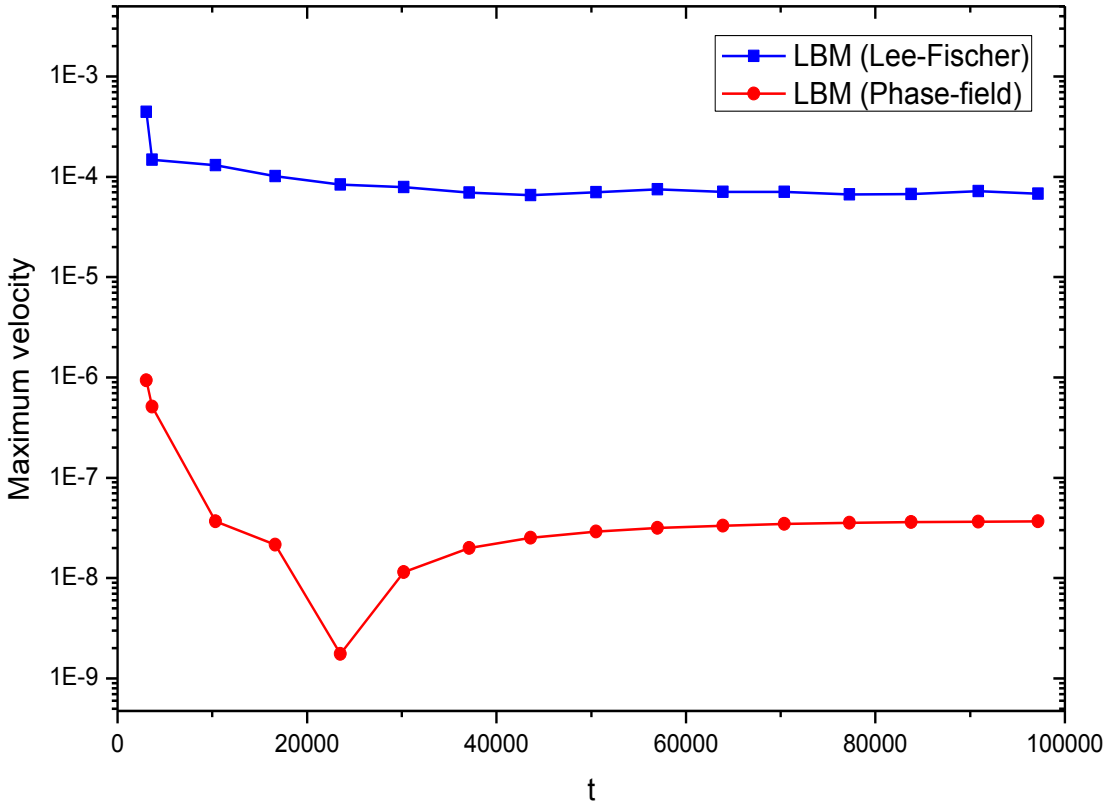

Figure 5. The time evolution of the maximum velocity for a single bubble.

Figure 6 presents the pressure variations with a function of radius for three different surface tensions in the stable state. Stationary bubbles with different radii are generated in the domain. It is seen that the LBM results are in good agreement with the theoretical solutions plotted by the solid lines.

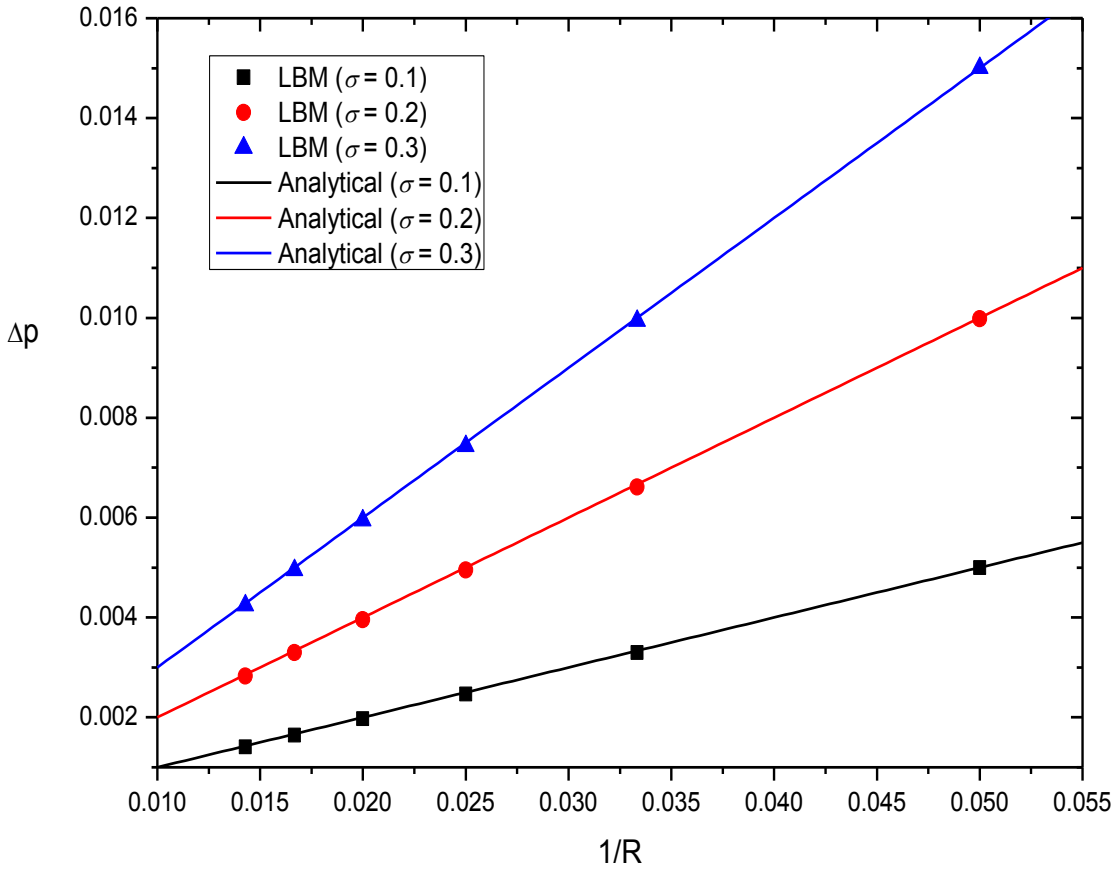

Figure 6. Variation of pressure with different radii for three different surface tension values.

To study the effect of the interface layer thickness parameter (W), several simulations have been performed with W as 1, 2, 3, 4, 4.5, 5, 5.5, and 6. Figure 7 shows the bubble with initial state.

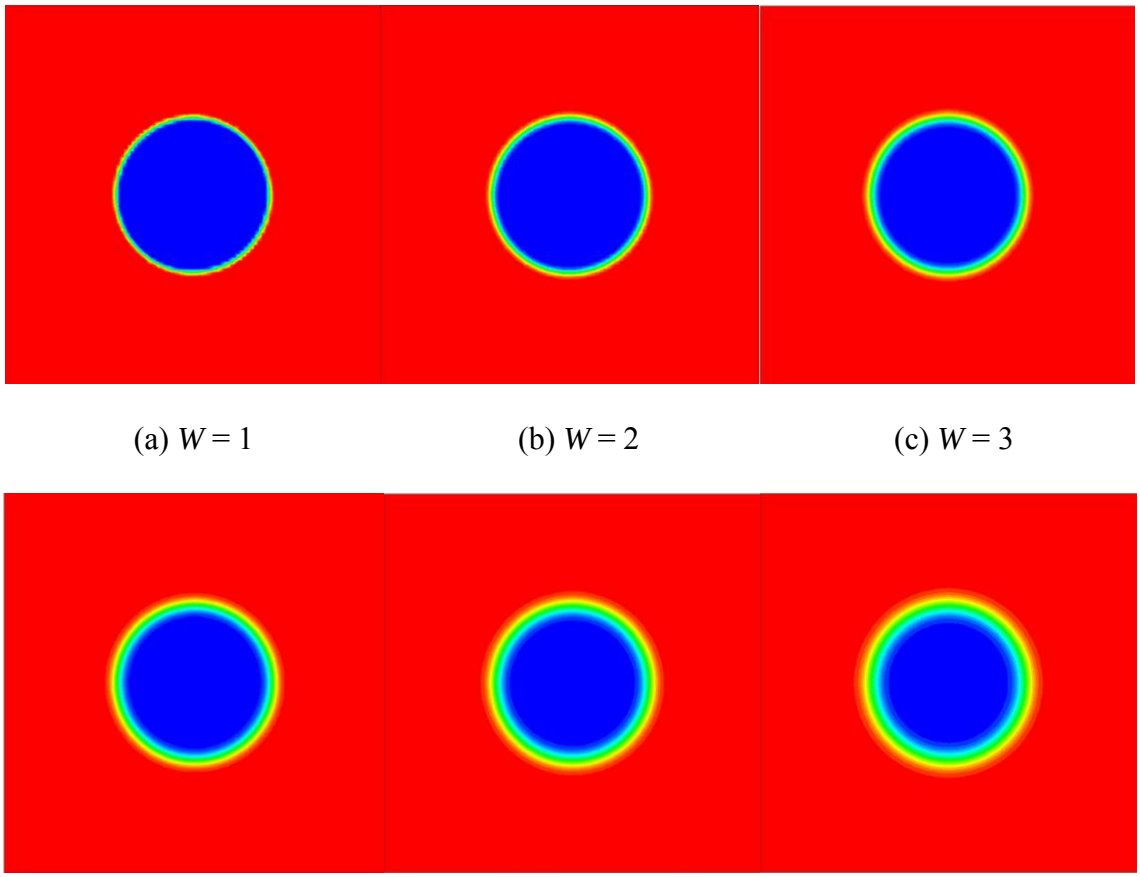

(a) $W = 1$ (b) $W = 2$ (c) $W = 3$

(d) $W = 4$ (e) $W = 5$ (f) $W = 6$

Figure 7. Interfacial thickness for a single bubble at the initial state.

As can be seen in Figure 8, it can be seen clearly that the numerical result approaches the analytical solution as the thickness of the interface layer increases. When the interface layer width is bigger than 5, the numerical result changes very little and matches the analytical value. This is because the discretization error decreases with the interface layer [17].

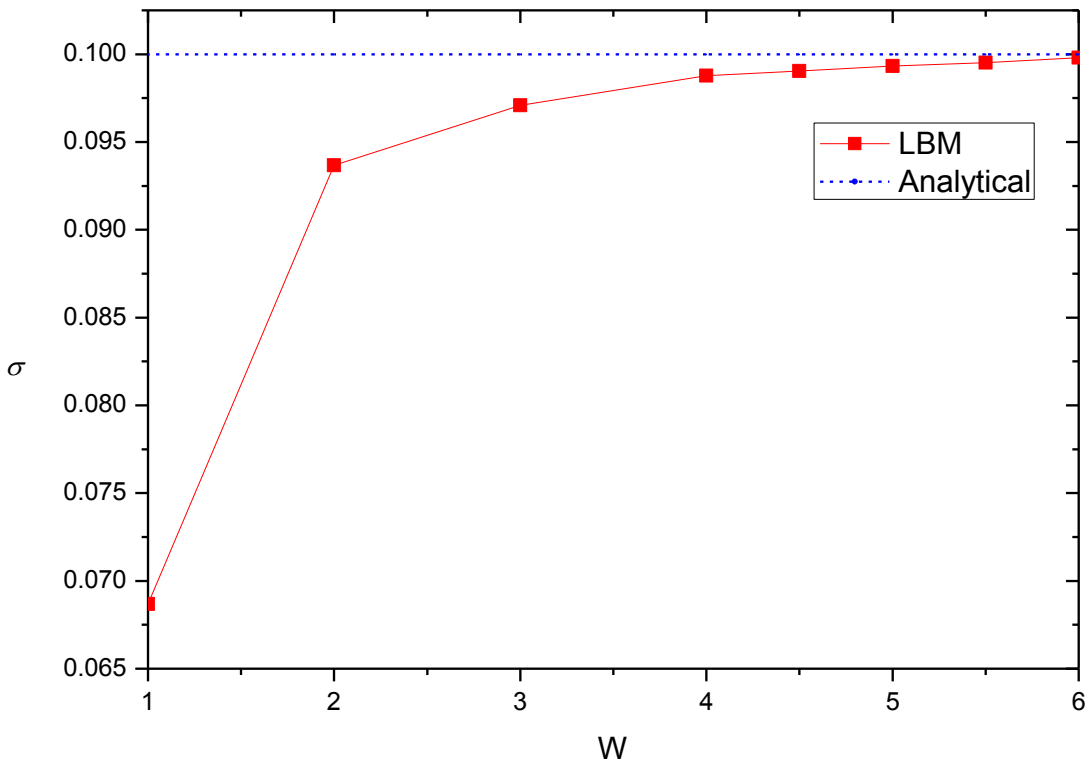

Figure 8. The influence of the varied interfacial layer width.

Figure 9 depicts the order parameter profile as a function of the radial distance from the center of the steady-state bubble with different interfacial layer thickness. As can be seen, the numerical results agree well with the analytical solution given by Equation (35) as the interfacial layer width increases. When the interface layer thickness is larger than 5, the numerical curve shapes match the analytical results very well.

A proper initial value of *W* for the stable and correct numerical simulation has to be chosen from the results of the numerical experiments. Of course, the method of

initialization may depend on the simulation problem. However, the initial condition closer to the equilibrium solution is recommended.

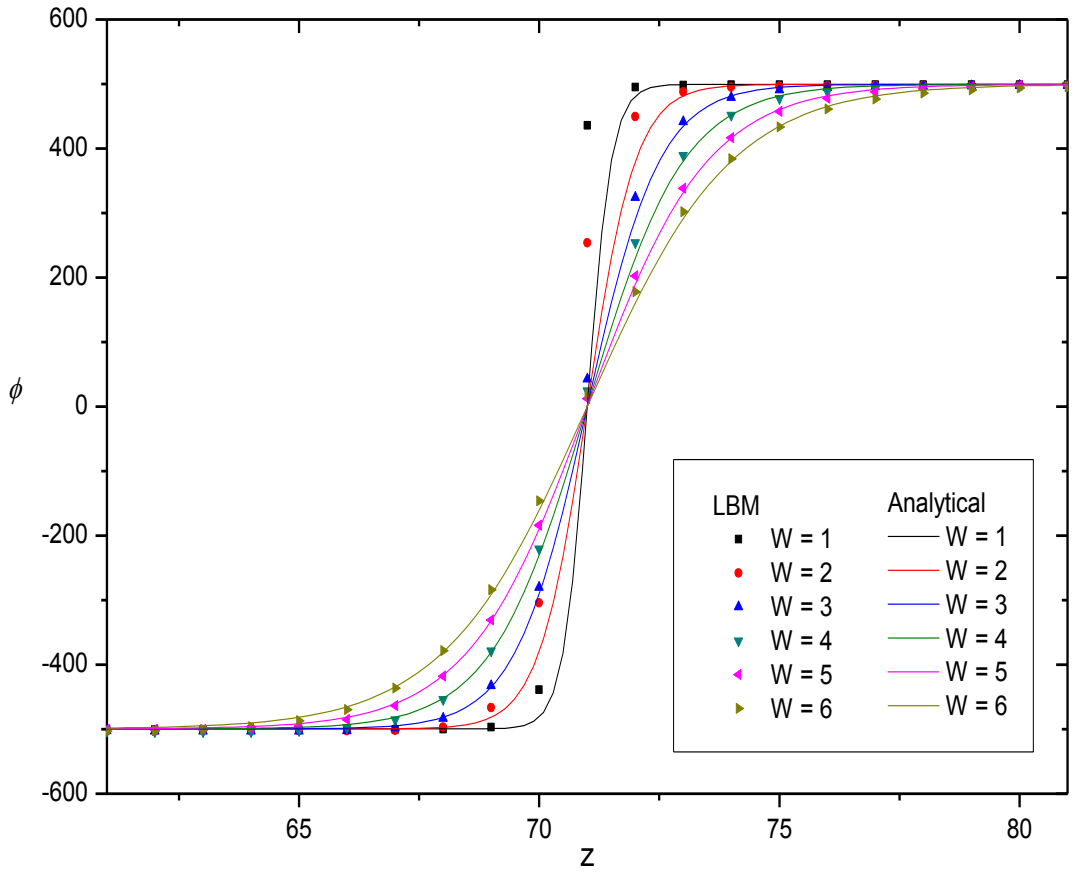

Figure 9. The order parameter profile along the interface of the stationary fluid.

In the LBM with phase-field modeling, the distribution of the initial order parameter (ϕ^*) from the phase densities plays an important role in the calculation. Figure 10 shows the initial bubble shape comparison of the initial bubble shape with or without the analytical order parameter distribution.

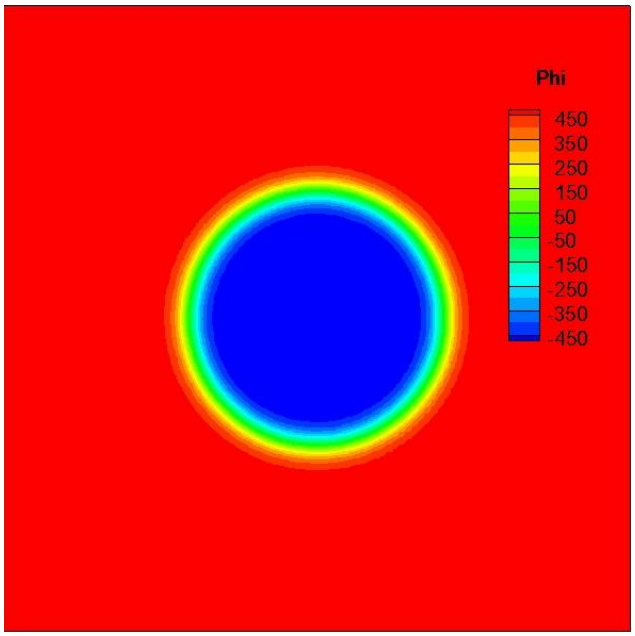

(a) With analytical solution

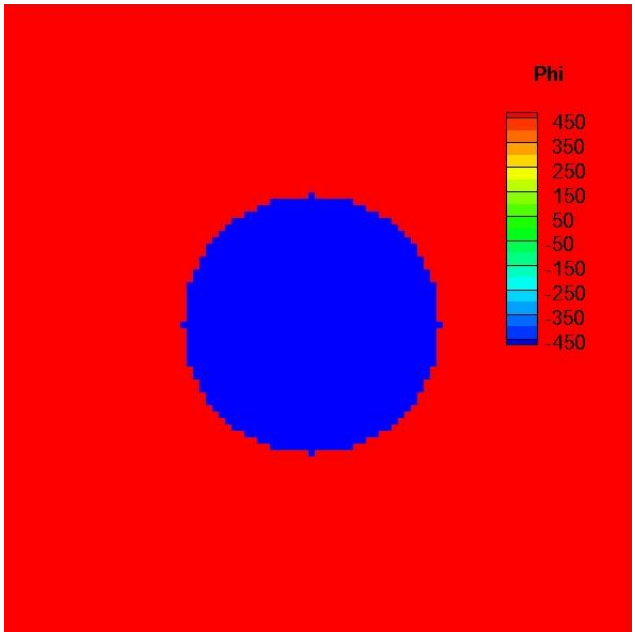

(b) Without analytical solution

Figure 10. The comparison of the initial order parameter distribution with or without the analytical solution for a two phase circular interface layer.

An improper initialization may increase the numerical fluctuation and instability across the interface layer and it can induce the error of pressure difference between the inside and outside of the bubble as Table 1 shows.

Table 1. The pressure difference between the inside and outside of the bubble.

Order parameter initialization	Numerical Δp	Theoretical Δp	Error in LBM (%)
Without analytical solution	5.82e-03	5.00e-3	+16.42
With analytical solution	4.97e-03	5.00e-3	-0.67

Due to the order parameter (ϕ), distribution is imperfect compared with the analytical solution; the radius of the bubble fluctuates during the initial period because of curvature effects needing accommodated.

The time variation of the bubble radius at the different initial interface conditions are shown in Figures 11 and 12, respectively. From these figures, it is obvious that the bubble radius with analytical order parameter initialization recovers its initial value at the steady-state, and that the fluctuation of the radius is smaller than without analytical order parameter initialization.

Conversely, the bubble radius without analytical order parameter initialization is reduced to 0.9984 from the initial radius ratio of 1.

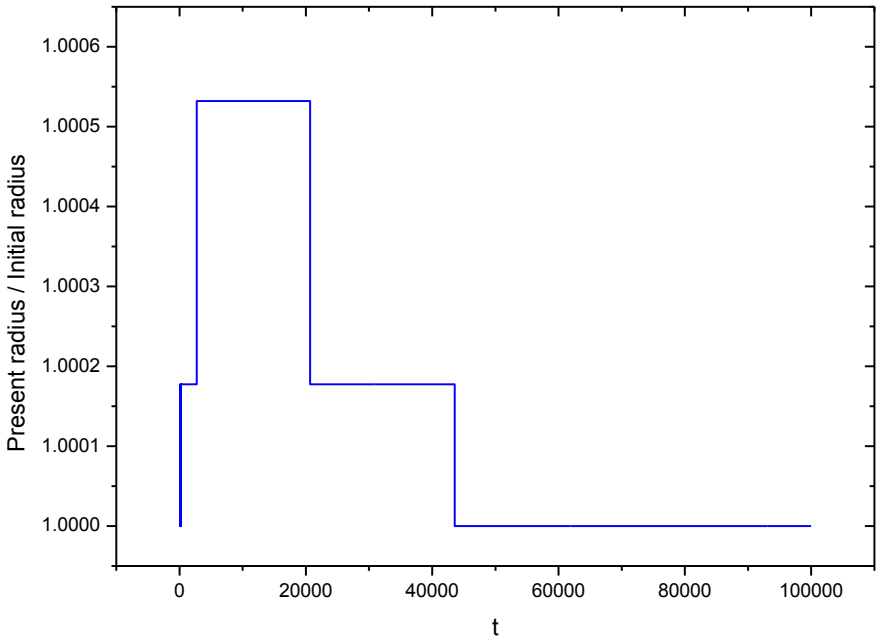

Figure 11. Time evolution of the bubble radius ratio with analytical order parameter.

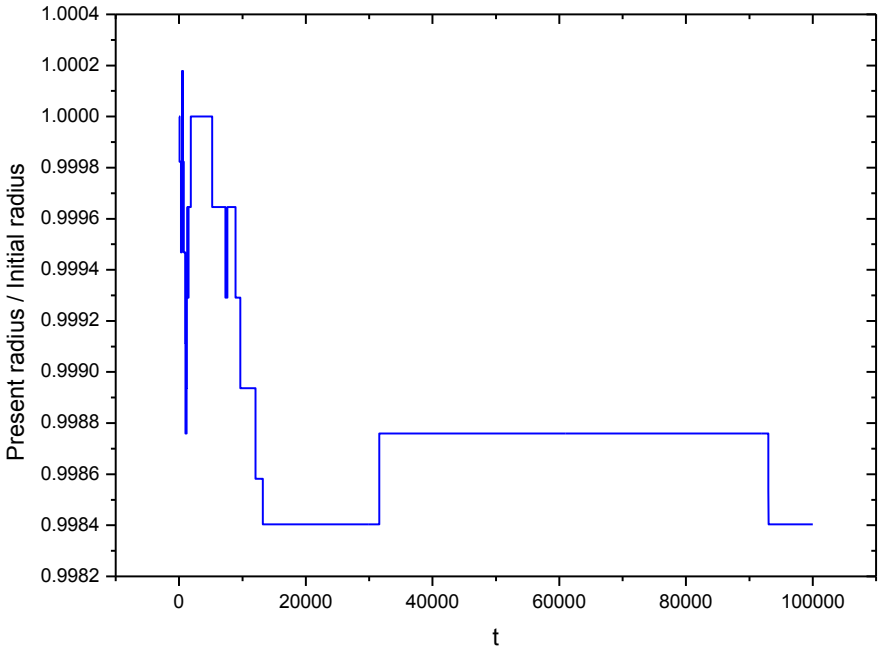

Figure 12. Time evolution of the bubble radius ratio with non-analytical order parameter.

Moreover, the order parameter distribution without analytical solution can generate larger spurious velocities than the distribution by analytical solution can, as shown in Figures 13 to 14. With the non-analytical solution order parameter distribution, the maximum velocity is increased from 10^{-8} to 10^{-7} by.

According to the verification of the order parameter distribution with or without analytical solution, the order parameter should be initialized with the analytical result not to produce any large fluctuations, which can lead to numerical instability.

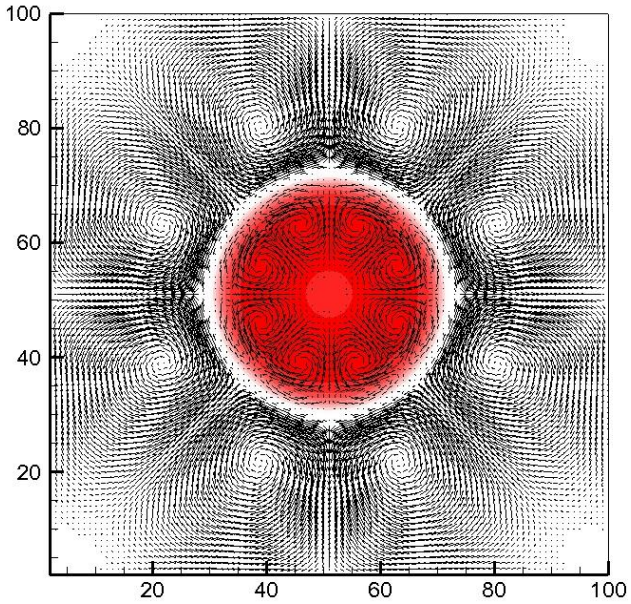

Figure 13. The velocity field for a single bubble without analytical solution order parameter initialization at the steady state.

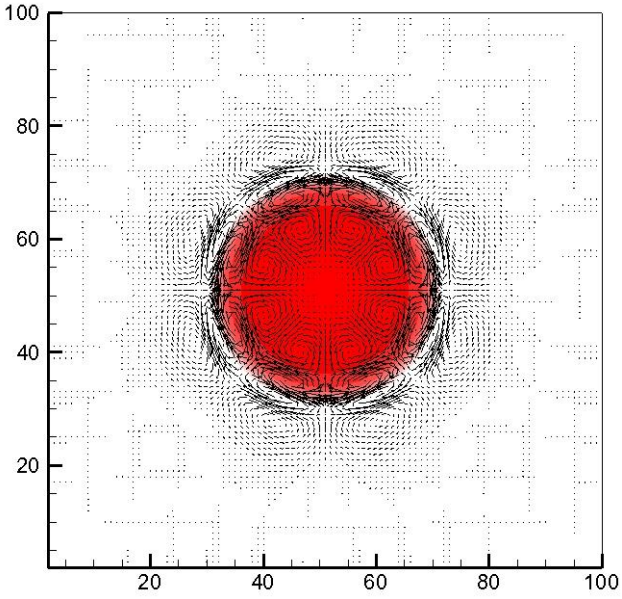

Figure 14. The velocity field for a single bubble with analytical solution order parameter initialization at the steady state.

Capillary wave

While the test of a single bubble in the stationary liquid bubble allows us to verify the equilibrium state, the simulation of the capillary wave can provide another effective way to test the interfacial dynamics. In this test, we can validate the capability of the LBM with phase-field modeling with a moving interfacial layer.

In this simulation, a sinusoidal interface in the middle separates a rectangular domain. Two different fluids with high-density ratios (1000) are located vertically across the interface.

If a plane interface is deformed in a wave-like manner, the order parameter will be distributed along the interfacial layer. The order parameter difference can induce positive and negative pressures, which will arise on the interface different sides. Under the influence of the surface tension and viscous forces, the interface undergoes a damped oscillation in the viscous fluid.

Here, the order parameters are initialized as a sinusoidal curve around $y = NY/2$ of one wave length NX,

$$\phi = \phi^* \tanh\left[\frac{2}{W}\left(y - \frac{NY}{2} - a\sin\kappa_w x\right)\right], \tag{36}$$

where a is the initial amplitude.

$$\frac{a}{NY} = \text{constant}, \tag{37}$$

and κ_w is the wave number

$$\kappa_w = \frac{2\pi}{\lambda} = \frac{2\pi}{NX}. \tag{38}$$

Here, *NX* and *NY* are the width and height of the domain, respectively.

At each time step, the height of the interface layer is measured. Since the position of the interface may not lie on the grid point, the interpolation method is chosen

$$y = iy - \frac{\phi(iy)}{\phi(iy) - \phi(iy-1)}, \tag{39}$$

where

$$\phi(iy)\phi(iy-1) < 0. \tag{40}$$

From the position of the interface layer, we can measure the time difference between the neighboring peak points, and calculate the oscillation period. Then, the numerical angular frequency can be calculated by

$$\omega = \frac{2\pi}{T}, \tag{41}$$

where ω and T are the angular frequency and the oscillation period, respectively.

Chandrasekhar gave an analytic solution for the case of two separated fluids with the same kinematic viscosity. In the long-wavelength limit, the decay rate and the oscillating frequency of an initially disturbed interface in the form of a sinusoidal perturbation could be calculated by taking the real and imaginary parts of the following relation, respectively

$$n = \kappa_w^2 \nu \left(y^2 - 1\right). \tag{42}$$

where y is the physically meaningful roots of the following equation,

$$y^4 + 4\alpha y^3 + 2(1-6\alpha)y^2 - 4(1-3\alpha)y + 1 - 4\alpha + s = 0\,, \tag{43}$$

in which

$$\alpha = \frac{\rho_H \rho_L}{(\rho_H + \rho_L)^2},\ s = \frac{\sigma}{\kappa_w (\rho_H + \rho_L)\nu^2}\,. \tag{44}$$

Different fluids are located the upper and lower side from the middle of domain. The mesh size is taken as 64 × 256. The bounce-back boundary condition is employed on the upper and lower walls, and the x-direction boundary condition is periodic. The same viscosity is used in the two phases to satisfy the prerequisite of the analytical solution. The densities are set to be ρ_H = 1000, and ρ_L = 1. The mobility coefficient (Γ) is chosen as 0.1. The single relaxation time is set as τ_n = 0.6 and τ_ϕ = 0.8, respectively. The parameter *W* is set to 5; and the *a*/*NY* is 0.02. The surface tension coefficient (σ) is taken as 0.521. We adopt the order parameter profile along interfacial layer given by the Equation (36).

The two-phase fluids can be divided by the order parameter distribution as shown in Figure 15. Due to the sinusoidal perturbation along the interface layer, the pressure difference can be generated as shown in Figure 16. As the time step progresses, the surface tension and viscous forces dampen the interfacial layer to the equilibrium state by as shown in Figure 17.

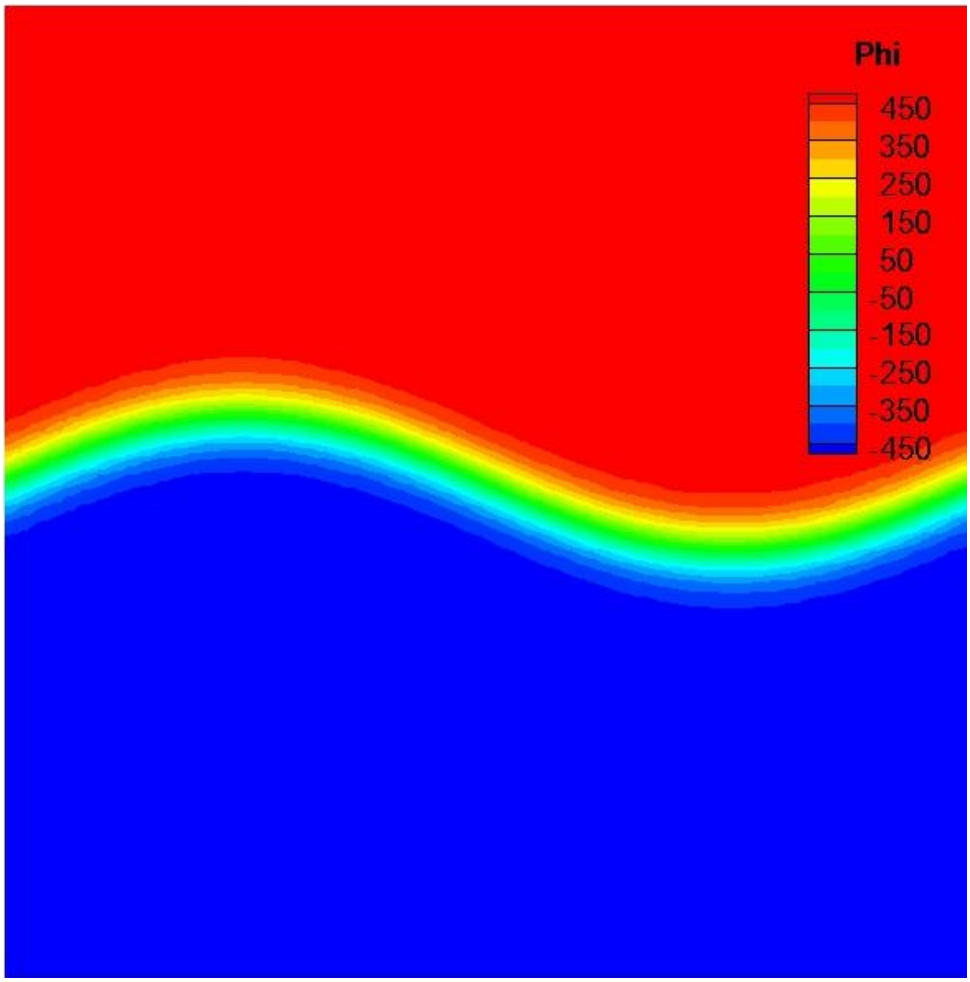

Figure 15. The order parameter distribution along the interfacial layer.

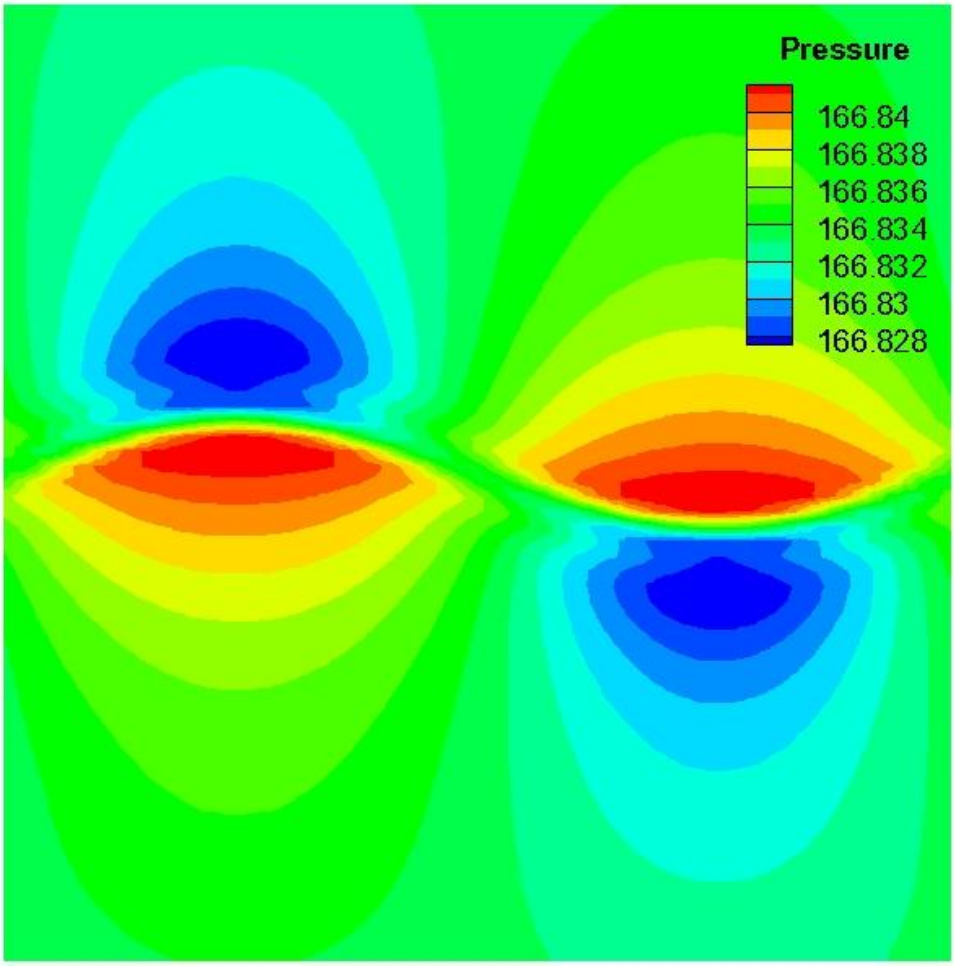

Figure 16. The pressure difference on the plane interface layer.

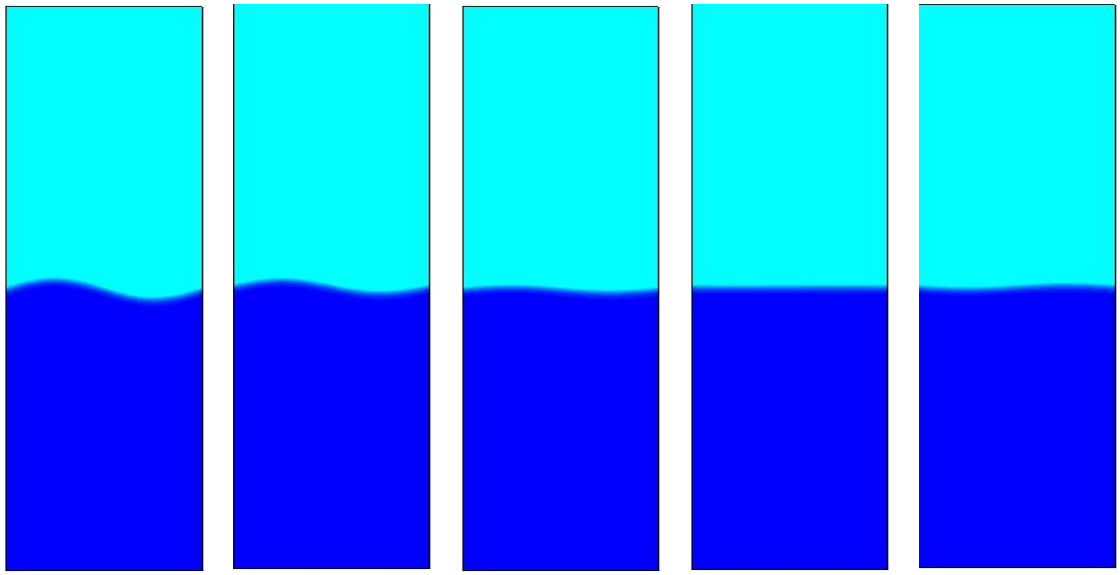

(a) t = 1000 (b) t = 2000 (c) t = 3000 (d) t = 4000 (e) t = 5000

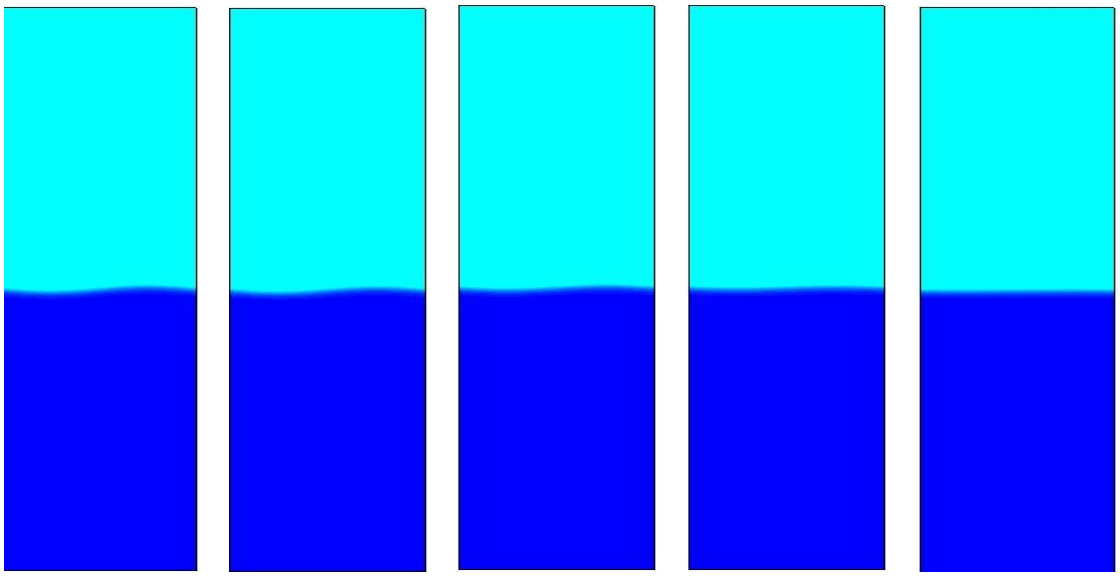

(f) t = 6000 (g) t = 7000 (h) t = 8000 (i) t = 9000 (j) t = 10000

Figure 17. The process to the equilibrium state of the capillary wave.

From the given parameters, we can calculate the angular frequency of the capillary wave as shown in Table 2. As can be seen, the simulation values agree well with the theoretic results.

Table 2. The angular frequency of capillary wave.

ω (LBM)	ω (Theory)	Error in LBM (%)
4.9307E-04	4.9389E-04	-0.1655

To investigate the effect of mobility coefficient Γ, we adopt various Γ as 0.02, 0.1, 1, 50, 100, and 200. Figure 18 depicts that as Γ is decreased the numerical values of the angular frequencies agree with the analytic results. However, very small Γ will cause numerical instability.

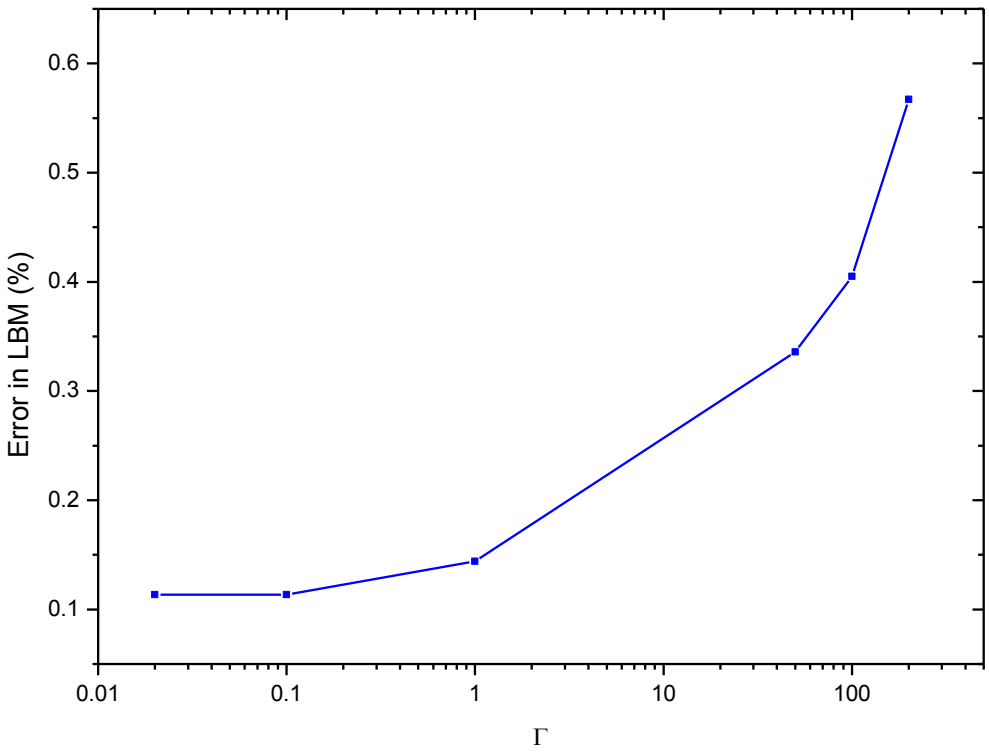

Figure 18. The LBM error with varied Γ of the capillary wave.

The coalescence of two droplets (or bubbles)

The coalescence of droplets (or bubbles) arises in many physical situations, including boiling, rain, emulsions, ink-jets, and many two-phase fluids. In this subsection, we will show that the LBM can be used to simulate the fundamental phenomena of the coalescence.

We consider two stationary liquid droplets (or bubbles) without collision in the two-dimensional domain. The density ratios of droplet to vapor and liquid to bubble are set to 1000.

When two droplets (or bubbles) come in contact, a connecting bridge is formed between them. Figure 19 shows the experimental image for the coalescence of two water droplets [33].

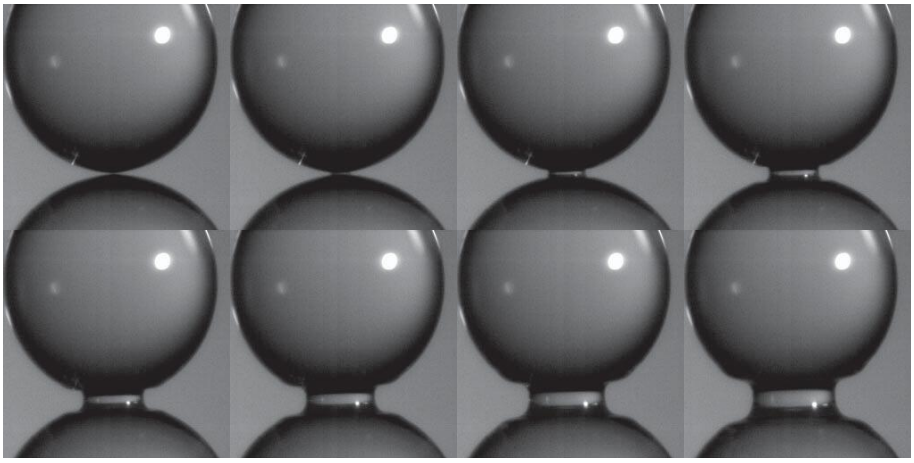

Figure 19. Experimental image of the coalescence of two water droplets.

Due to surface tension forces, the connecting bridge thickens rapidly. The speed of the bridge increment originates from the mutual competition between the inertial forces driving coalescence and the viscous forces slowing it down [34].

The relationship between viscous and inertial force can govern the coalescence process. It can be characterized as the Reynolds number defined by

$$\mathrm{Re} = \frac{\rho\left(\frac{\sigma}{\mu}\right) r_b}{\mu}, \tag{45}$$

where ρ is the density of droplet; r_b is the radius of the connecting bridge; σ is the surface tension coefficient; and μ is the dynamic viscosity.

For Re < 1, the viscous force (viscous coalescence) dominates the coalescence, while for Re > 1, the inertial force (inertial coalescence) governs it. The crossover between viscous and inertial coalescence will occur at Re = 1.

For merging low viscosity droplets (or bubbles), the inertial coalescence is the dominant process. To evaluate the temporal evolution, bridge radius r_b and time t can be non-dimensionalized as

$$r^* = \frac{r_b}{R_0}, \tag{46}$$

$$t^* = \frac{t}{\tau_i}, \tag{47}$$

where R_0 is the initial droplet (or bubble) radius, which is assumed to be same for both droplets (or bubbles); and τ_i is the inertial time given by

$$\tau_i = \sqrt{\frac{\rho R_0^3}{\sigma}}. \tag{48}$$

Two circular water droplets (or bubbles) with radius R_0 are located vertically with a gap of d. The computational domain is adopted as $5R_0 \times 10R_0$. The periodic boundary condition is taken at all boundaries. The density ratio is set as 1000 ($\rho_H = 1000$, $\rho_L = 1$). The parameters are chosen as $R_0 = 20$; $\sigma = 0.1$; $\tau_n = 0.6$; $\tau_\phi = 0.7$; and $\Gamma = 40$. The gap of the two bubbles (d) and the width of the interface (W) are set to 4.

Figures 20 and 21 show the coalescences of two droplets and bubbles. Due to the intermolecular attraction, the two droplets (or bubbles) generate a bridge. Then, the surface tension force widens the bridge. At the steady-state, the shape of the two droplets (or bubbles) turns into the circle.

Figure 22 depicts the comparison of the variation of the non-dimensional bridge radius r^* as a function of the square-root of the non-dimensional inertial time t^* between the present LBM result and the experiment for low viscosity fluids [35]. The non-dimensional bridge of droplets is proportional to non-dimensional inertial time as shown in Figure 22 for the simulation and experimental results. The simulation result agrees well with the experimental data.

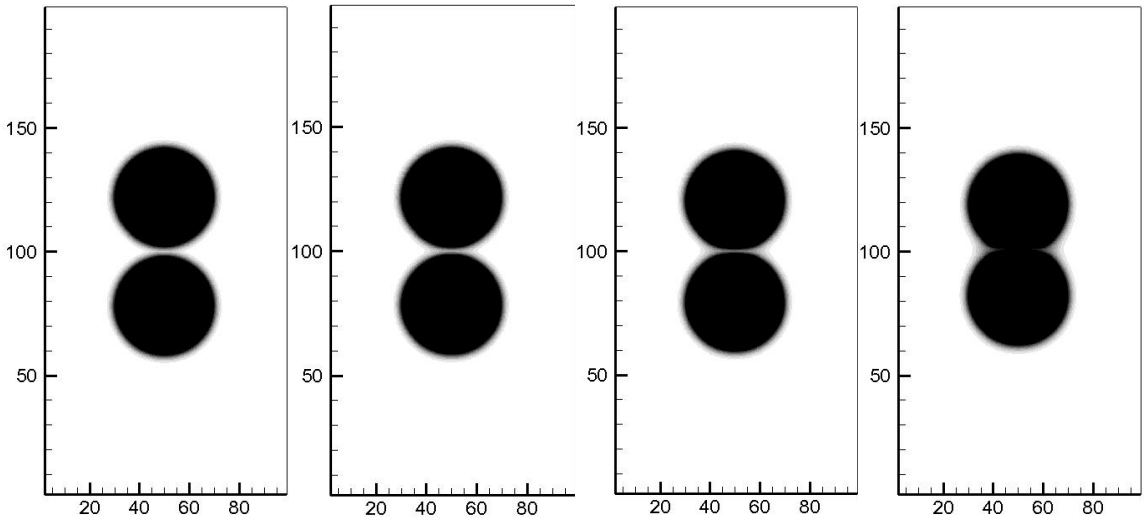

(a) t = 10000 (b) t = 50000 (c) t = 100000 (d) t = 150000

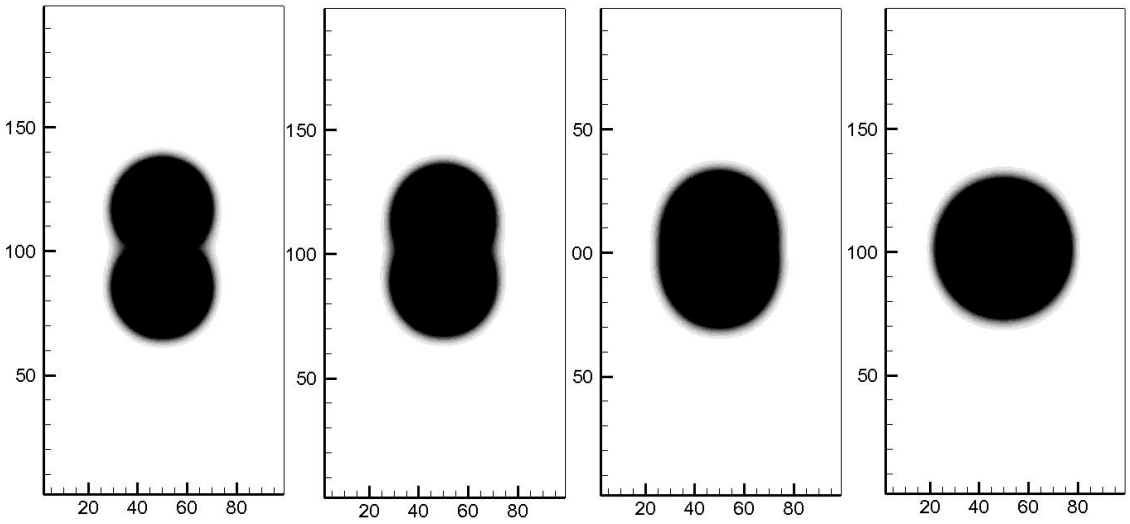

(e) t = 180000 (f) t = 200000 (g) t = 220000 (h) t = 300000

Figure 20. The coalescence of two stationary droplets.

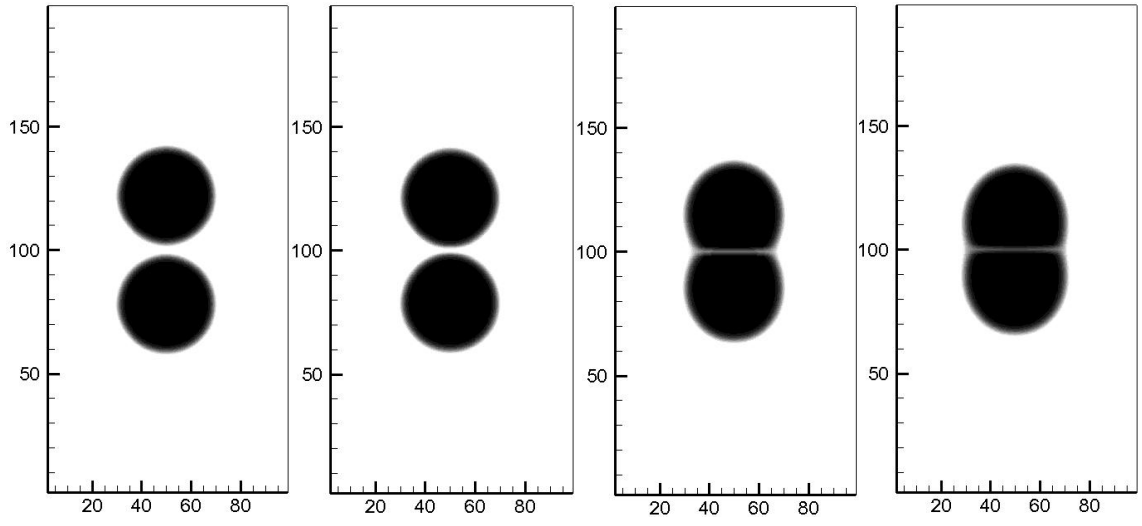

(a) t = 10000 (b) t = 50000 (c) t = 100000 (d) t = 110000

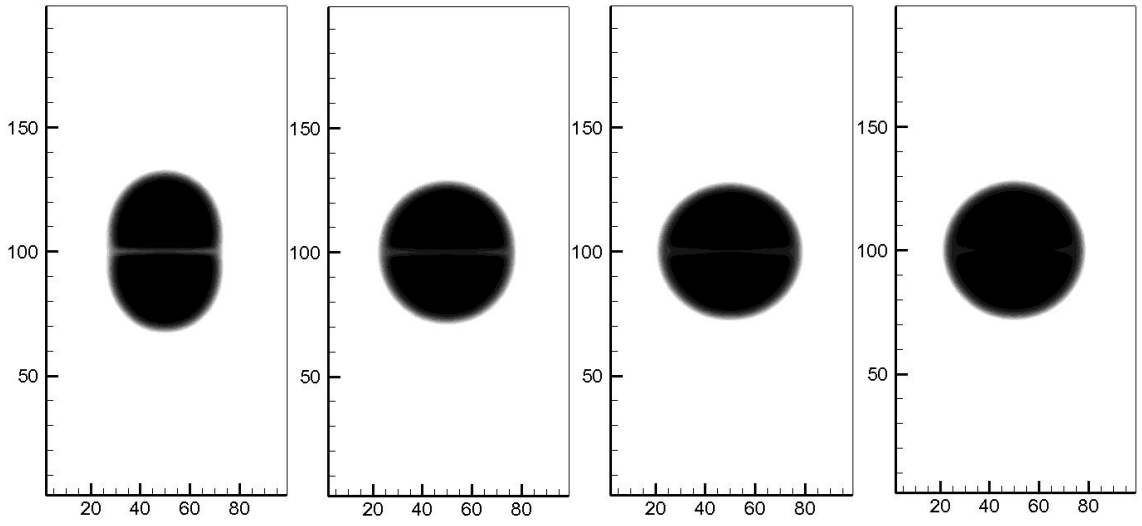

(e) t = 120000 (f) t = 150000 (g) t = 200000 (h) t = 300000

Figure 21. The coalescence of two stationary bubbles.

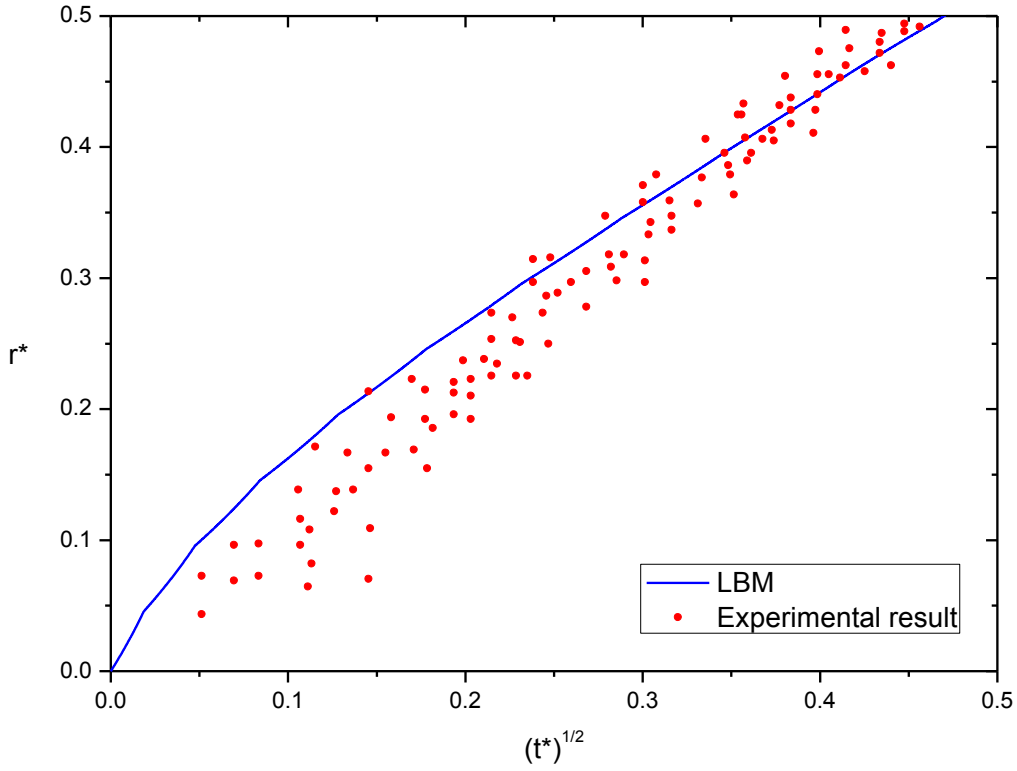

Figure 22. The variation of the non-dimensional bridge radius r^* as a function of the square-root of the non-dimensional inertial time t^* for low viscosity fluid.

Next, to study the effect of the mobility coefficient on the initial contacting time step, Γ is set to 10, 20, 40, 80, 160, and 320 for the droplets and bubbles, respectively. The other parameters remain unchanged.

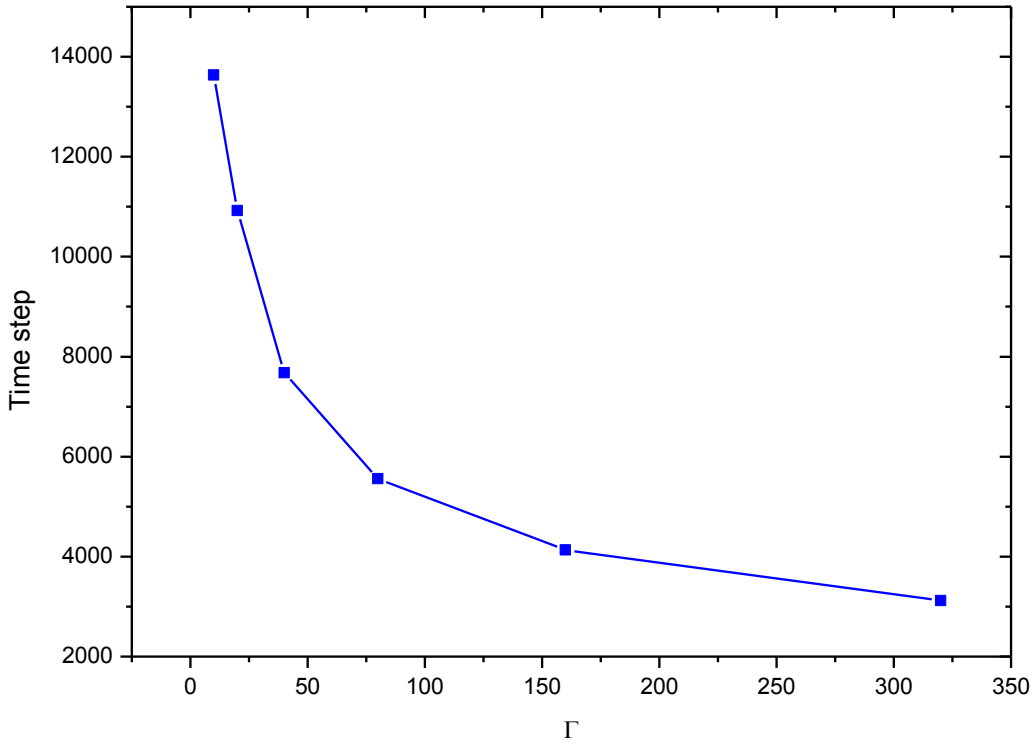

Figure 23. The initial contacting time step with various Γ.

The simulation results of the droplets and bubbles show exactly the same value. As the mobility coefficient (Γ) is increased, the initial contacting time step between bubbles is reduced because the large Γ (Figure 23) can effect the diffusivity of the bubbles interfacial layer.

A single bubble rising under buoyancy

As a fundamental subject of bubble dynamics, many researchers have simulated the two dimensional single bubble under buoyancy [24, 36-44]. However, there are still unresolved questions about the flow field surrounding the bubble.

We simulate two-dimensional, two-phase fluid motions under gravity. The experimental results for a single rising bubble are usually communicated by some non-dimensional parameters, which characterize the rising bubble dynamics. The important dimensionless parameters are Eötvös number, Morton number, and Reynolds number [24]

$$Eo = \frac{g\left(\rho_H - \rho_L\right)D^2}{\sigma}, \tag{49}$$

$$M = \frac{g\left(\rho_H - \rho_L\right)\nu_H^4}{\sigma^3}, \tag{50}$$

$$\mathrm{Re} = \frac{u_T D}{\nu_L}, \tag{51}$$

where g is the gravitational acceleration; D is the bubble diameter; ν_L is the kinematic viscosity of the high density phase; and u_T is the terminal velocity of the rising bubble Hereafter, the effect of body force to bubble regime is defined by,

$$\mathbf{F}_b = -g\Delta n, \quad \text{where } \phi < 0, \tag{52}$$

in which Δn is the number density difference and the gravitational acceleration in pointing downward. The bubble will rise at a nearly constant velocity as the balance between the buoyancy and drag force. In fact, the velocity of the bubble is not constant

because there are some oscillations during the rising process. The bubble velocity is calculated by

$$\mathbf{u}_{bubble} = \frac{\sum \phi \mathbf{u}}{\sum \phi} \text{ ,where } \phi < 0. \tag{53}$$

To study the properties of the bubble with various density ratios, two types of simulation are conducted with a low and high-density ratio, respectively. In the first test, stationary walls surround the bubble. The bubble radius (R) and the domain size are set as 10 and 8R × 30R, respectively. The bubble is located at the lower region (quarter of the height) of the computational domain. The Bounce-Back boundary condition is specified on the bottom and top walls of domain and the horizontal side boundaries are assumed to be periodic. The density of each phase and the surface tension coefficient are the same as those used by Takada et al. [24], $\rho_H = 1.42$; $\rho_L = 0.58$; and $\sigma = 0.00521$. The parameters of the interfacial layer width (W) and the mobility parameter (Γ) are taken as 5 and 0.05, respectively. The initial order parameter is distributed by Equation (35) along the interfacial layer. The relaxation time parameters are set as $\tau_n = \tau_\phi = 0.0875$.

Next, we simulate a bubble rising case with a large density ratio. A bubble ($R = 30$) is located in the domain $30R \times 30R$. The initial center position of bubble is (450, 225). The boundary condition is same as the first test. The densities are set as $\rho_H = 1000$, and $\rho_L = 1$.The surface tension coefficient is taken as 2. The relaxation time and mobility parameter are chosen as $\tau_n = \tau_\phi = 0.959$, and 100, respectively.

To investigate the terminal velocity and the shape of the bubble in the first test (low density ratio), the several simulations are performed under different parameters as shown in Table 3.

Table 3. The parameters for the simulation of a bubble rising under buoyancy.

Cases	*Eo*	*M*	Gravity magnitude
1	5	0.2267	7.7529E-05
2	10	0.4535	1.5506E-04
3	20	0.9070	3.1011E-04
4	40	1.8134	6.2023E-04

In the second test, the varied Eötvös number and Morton number are taken to observe the properties of the bubble with a high-density ratio as shown in Table 4.
Due to the buoyancy force, the bubble will move upward. Meanwhile, the friction of surrounding fluid will deform the central part of the bubble. When *Eo* = 5, the shape of the bubble does not change too much. However, as *Eo* increases from 5 to 40, the bubble will deform more as shown in Figure 24. This is because the gravity magnitude (buoyancy force) will be proportional to the *Eo*.

Table 4. The parameters for the bubble rising simulation with large density ratio.

Cases	*Eo*	*M*	Gravity magnitude
5	15.984	0.6097	8.8889e-06
6	39.96	1.52425	2.2222e-05
7	79.92	3.0485	4.4444e-05
8	239.76	9.146	1.3333E-04

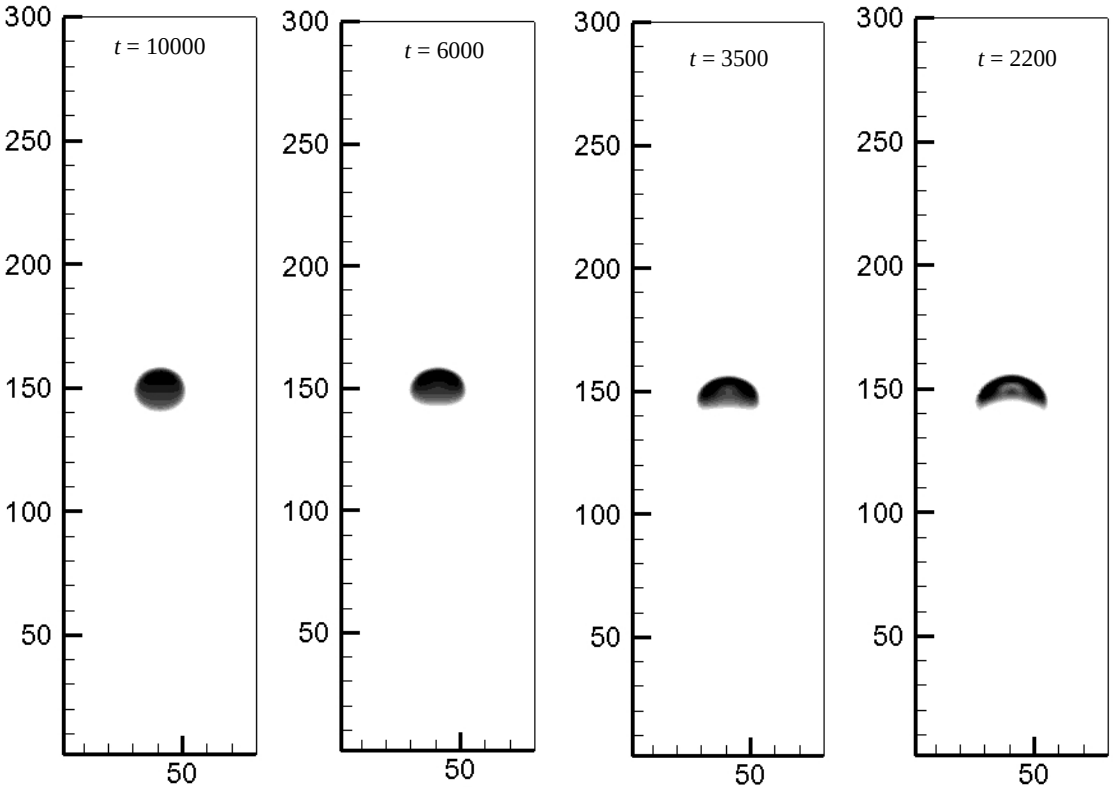

(a) Case 1 (b) Case 2 (c) Case 3 (d) Case 4

Figure 24. The bubble shapes under different conditions.

Table 5. The terminal velocity of a rising bubble with buoyancy.

Cases	u_T(present)	u_T(Takada)	u_T(VOF)
1	7.81e-3	7.82e-3	8.28e-3
2	1.35e-2	1.38e-2	1.43e-2
3	2.11e-2	2.17e-2	2.15e-2
4	3.28e-2	3.11e-2	3.08e-2

Table 5 shows the comparisons of the bubble terminal velocity with other numerical results. It can be easily observed that they agree well with the VOF method and Takada et al [24].

Figure 25 shows the terminal bubble shapes of four cases. The present results of shape agree well with the experimental findings of Crift et al. From this figure, it can be clearly observed that the bubble shapes gradually change from ellipsoidal to skirted. Equation (48) indicates the increase of *Eo* is equivalent to the increment of the gravity magnitude. Due to the buoyancy force associated with the gravity magnitude, the degree of deformity and the terminal velocity are increased.

For all the cases, a pair of vortices is formed inside bubble the first time. Then, the bubble refloats by the buoyancy force. Meanwhile on the bubble rising, the middle part of the bubble starts deforming due to the surrounding water. By the *Eo* increment, the flow patterns become more complex as shown in Figures 26 to 45. For all cases, the bubble is always kept symmetric and a wake flow is developed behind the bubble.

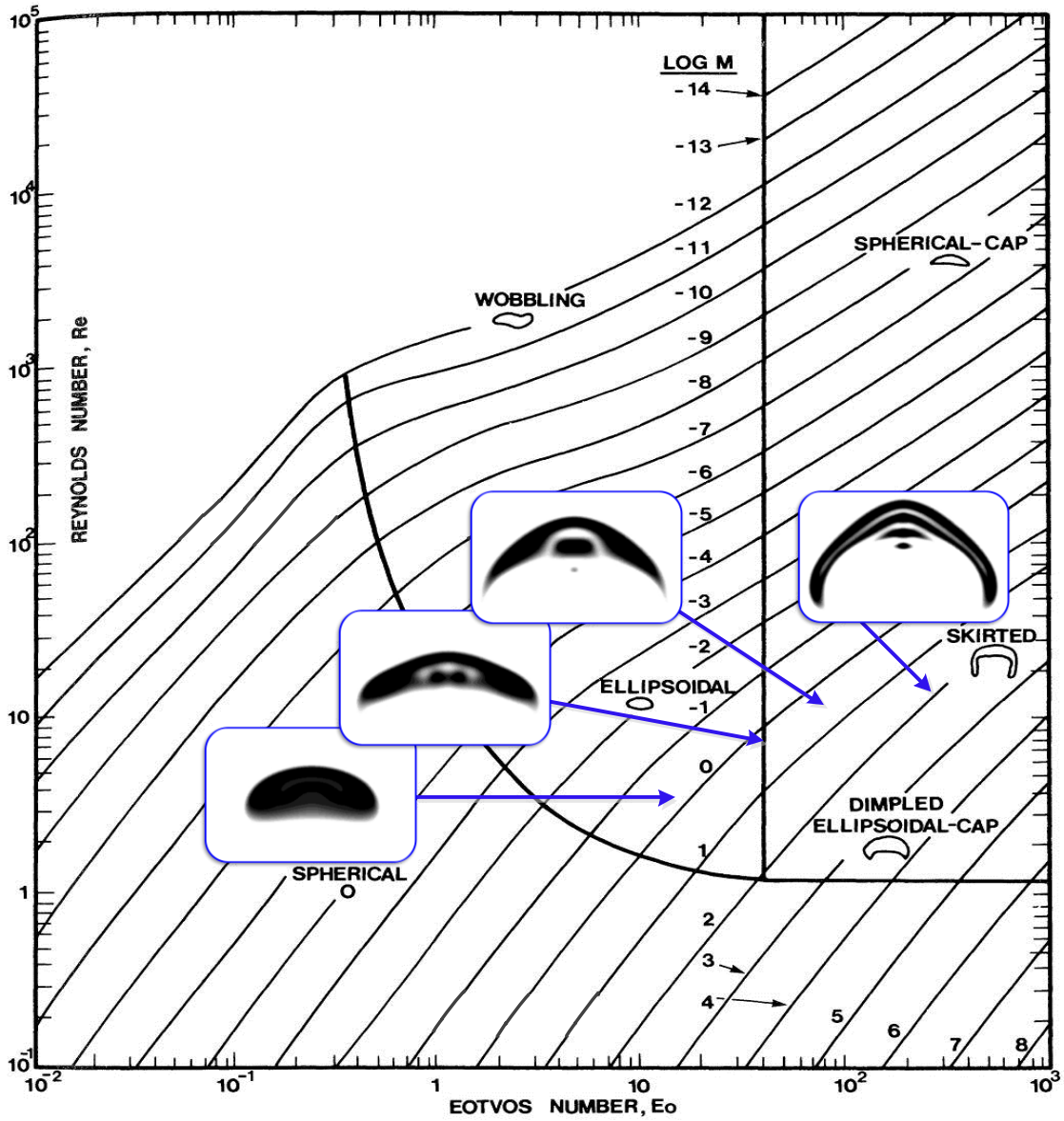

Figure 25. The comparison of bubble shape between the LBM and experimental results.

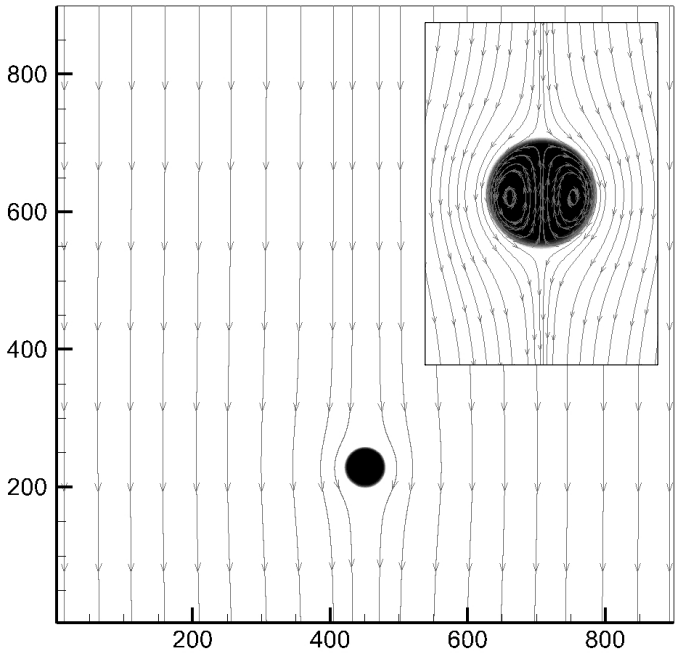

Figure 26. The flow pattern and shape of a bubble rising (case 5, t = 1000).

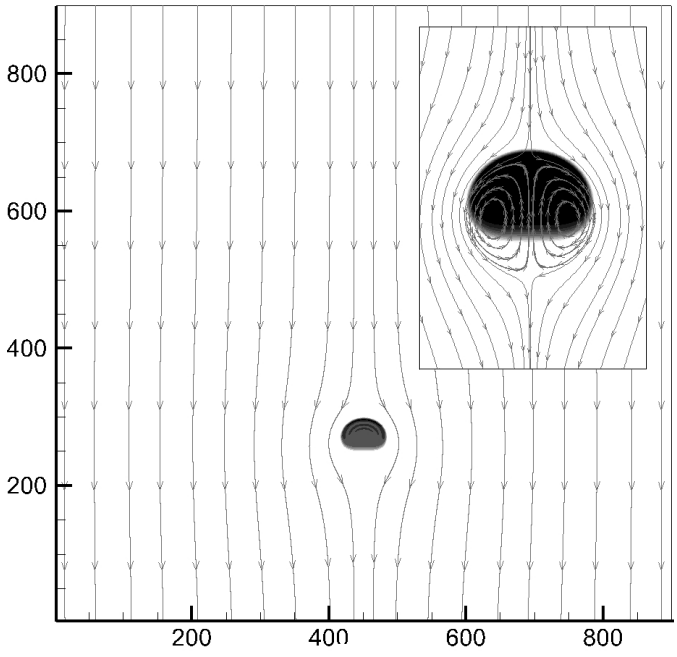

Figure 27. The flow pattern and shape of a bubble rising (case 5, t = 5000).

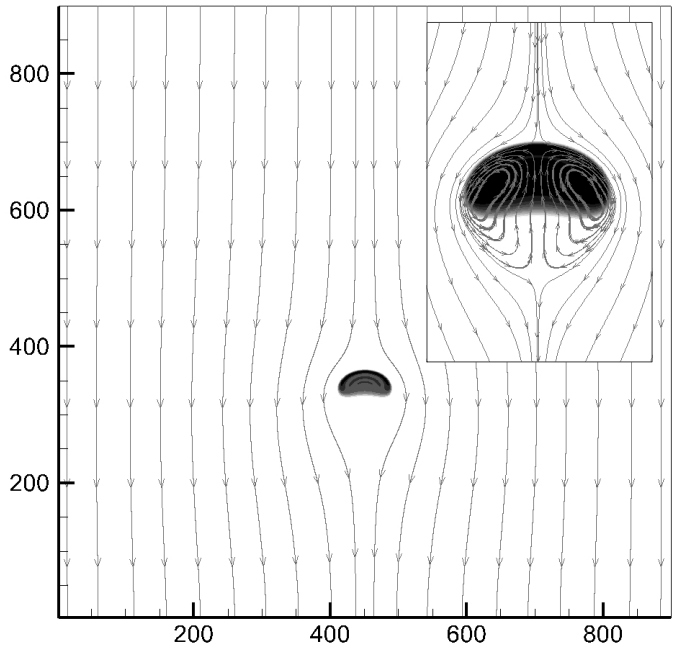

Figure 28. The flow pattern and shape of a bubble rising (case 5, t = 10000).

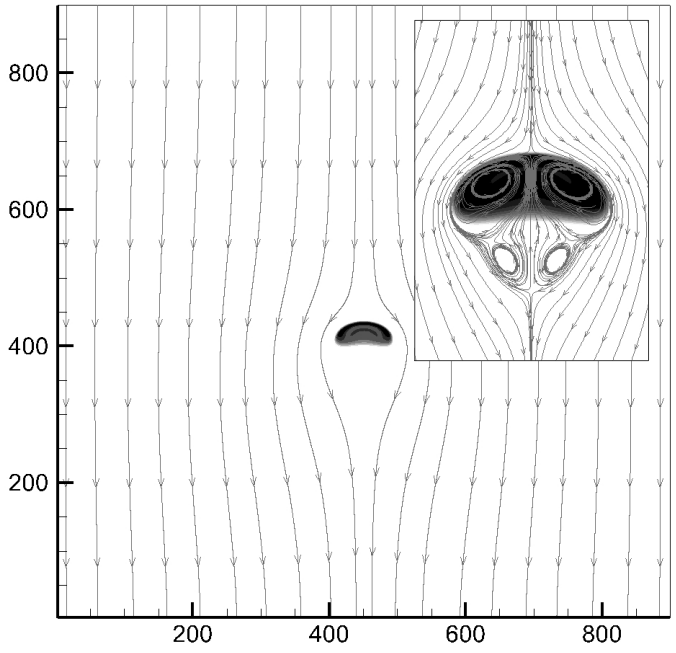

Figure 29. The flow pattern and shape of a bubble rising (case 5, t = 15000).

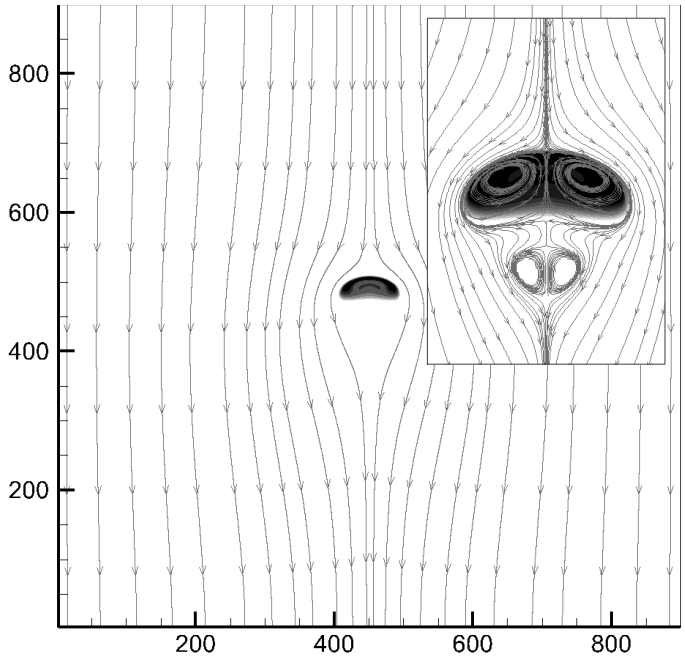

Figure 30. The flow pattern and shape of a bubble rising (case 5, t = 20000).

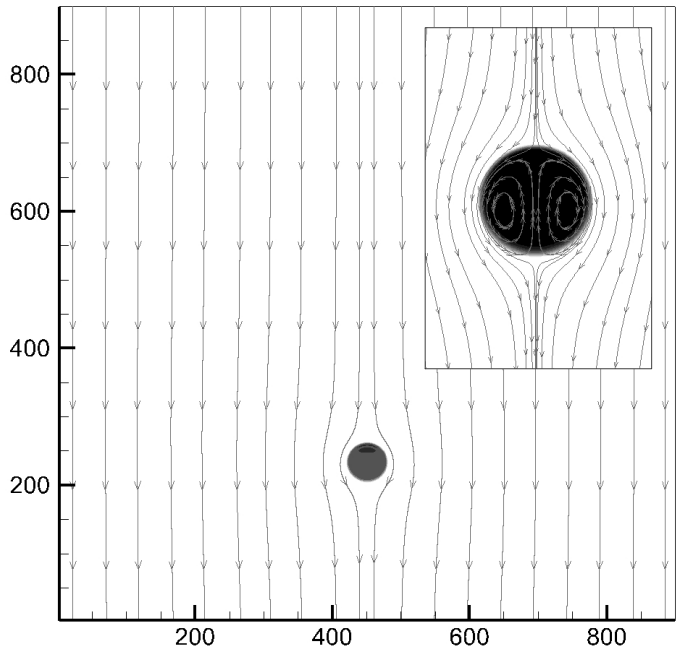

Figure 31. The flow pattern and shape of a bubble rising (case 6, t = 1000).

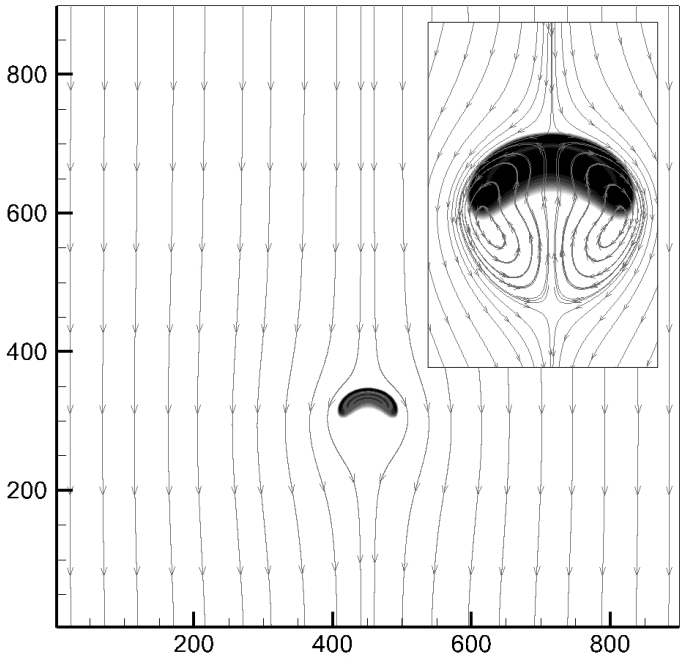

Figure 32. The flow pattern and shape of a bubble rising (case 6, t = 5000).

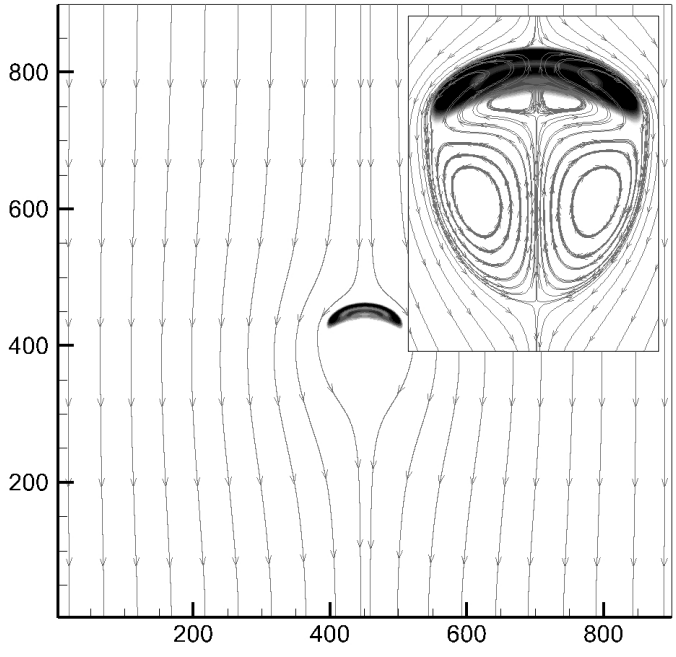

Figure 33. The flow pattern and shape of a bubble rising (case 6, t = 10000).

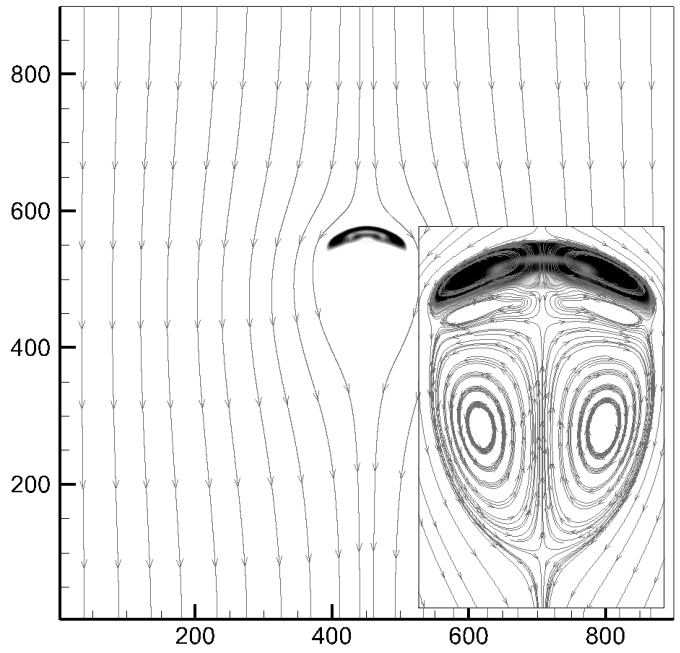

Figure 34. The flow pattern and shape of a bubble rising (case 6, t = 15000).

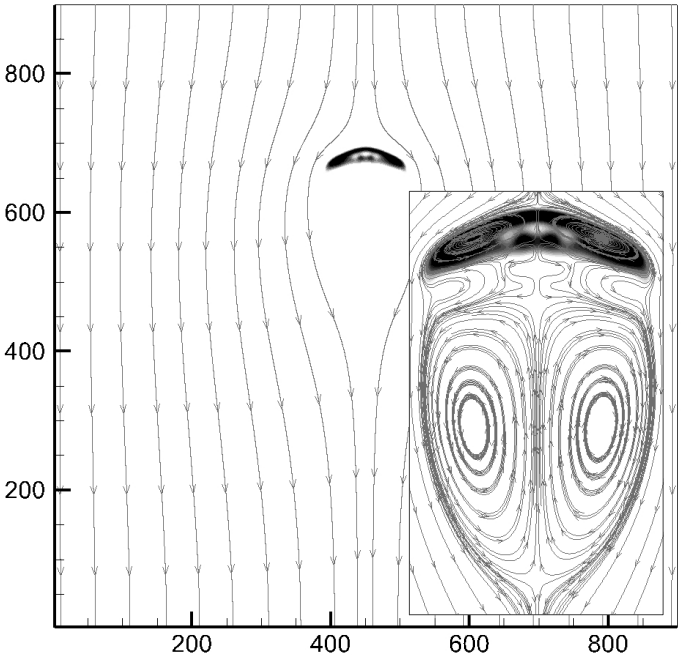

Figure 35. The flow pattern and shape of a bubble rising (case 6, t = 20000).

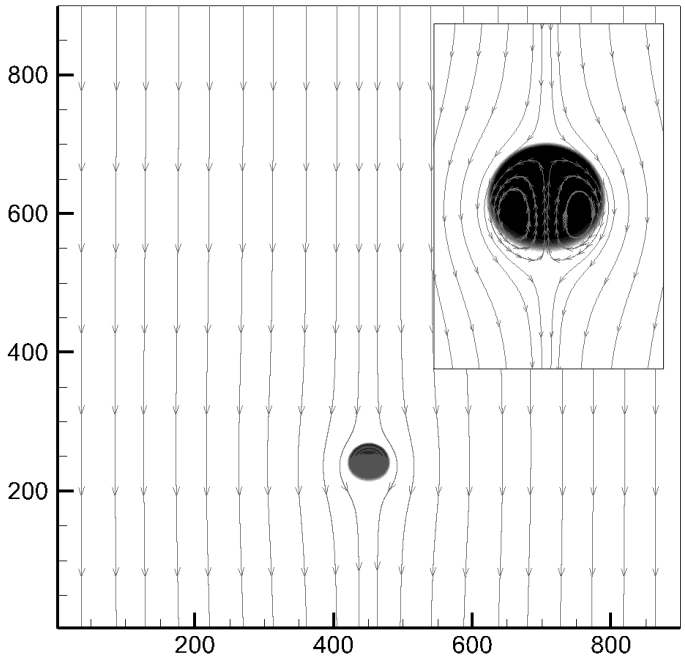

Figure 36. The flow pattern and shape of a bubble rising (case 7, t = 1000).

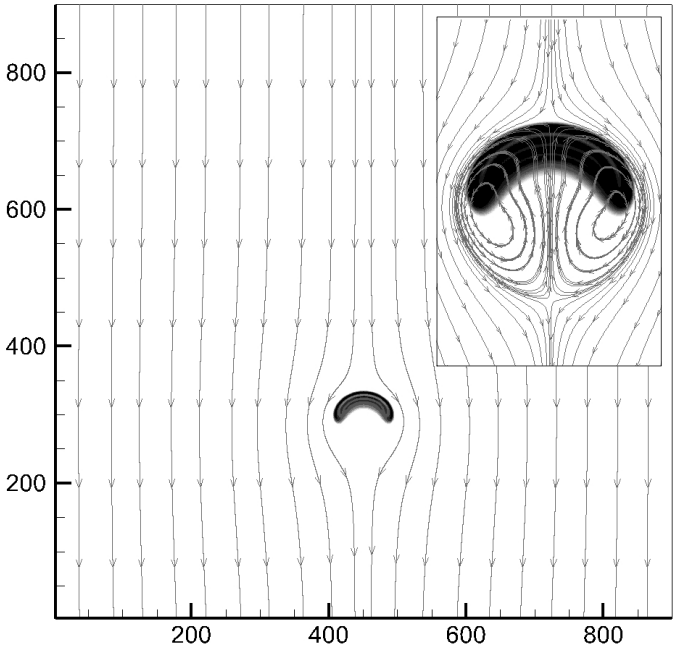

Figure 37. The flow pattern and shape of a bubble rising (case 7, t = 3000).

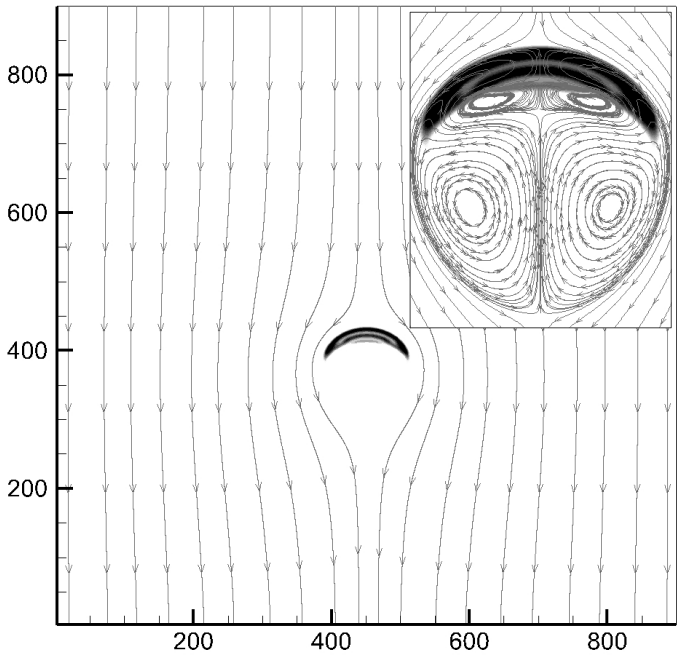

Figure 38. The flow pattern and shape of a bubble rising (case 7, t = 6000).

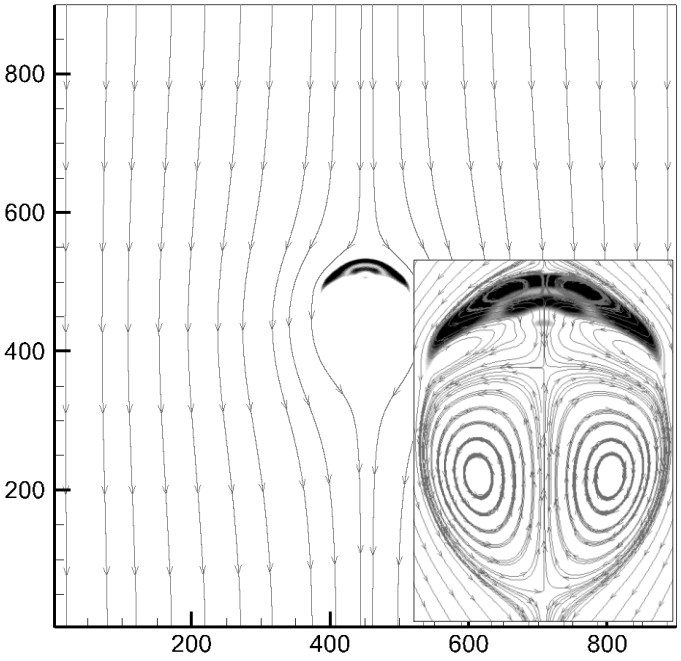

Figure 39. The flow pattern and shape of a bubble rising (case 7, t = 9000).

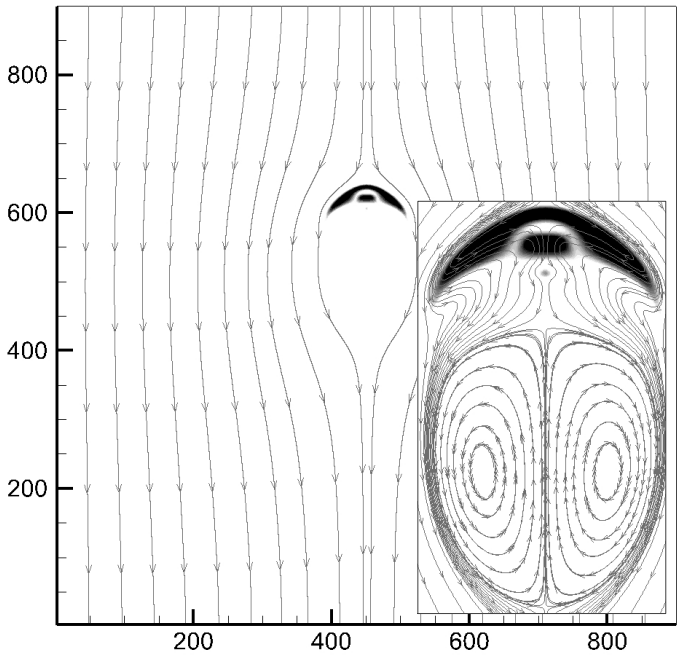

Figure 40. The flow pattern and shape of a bubble rising (case 7, t = 12000).

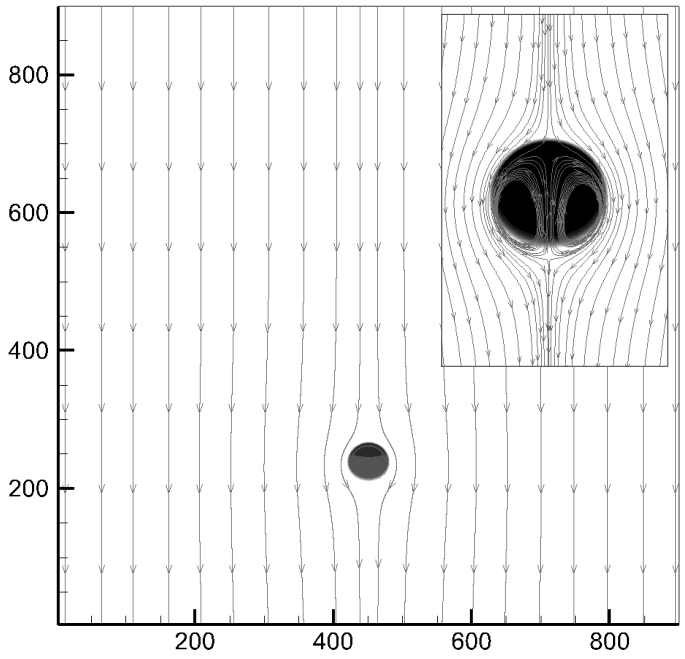

Figure 41. The flow pattern and shape of a bubble rising (case 8, t = 500).

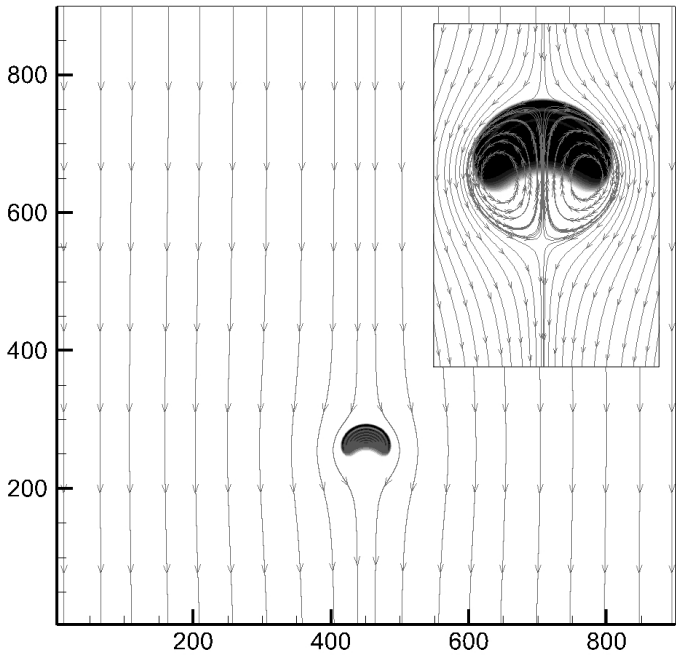

Figure 42. The flow pattern and shape of a bubble rising (case 8, t = 1000).

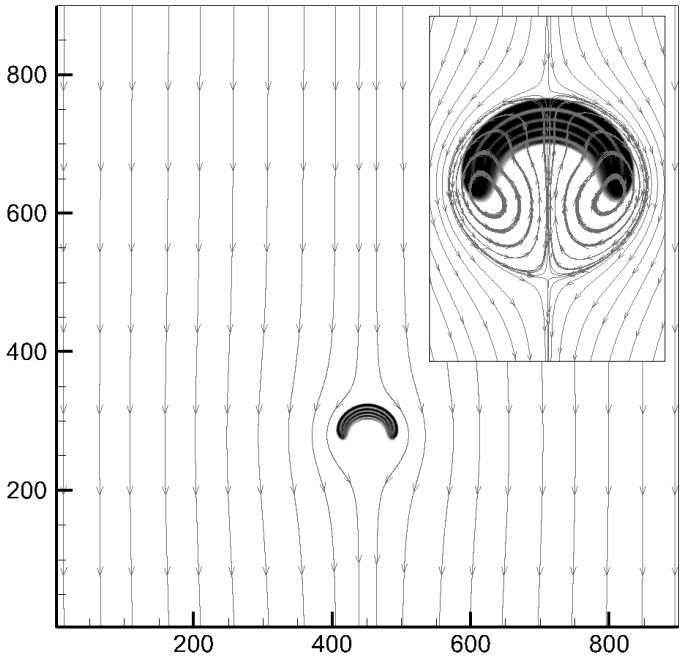

Figure 43. The flow pattern and shape of a bubble rising (case 8, t = 1500).

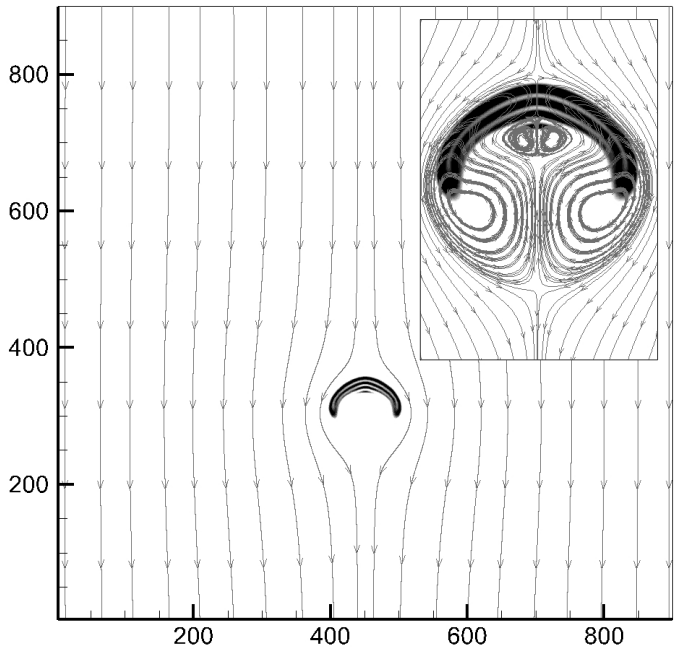

Figure 44. The flow pattern and shape of a bubble rising (case 8, t = 2000).

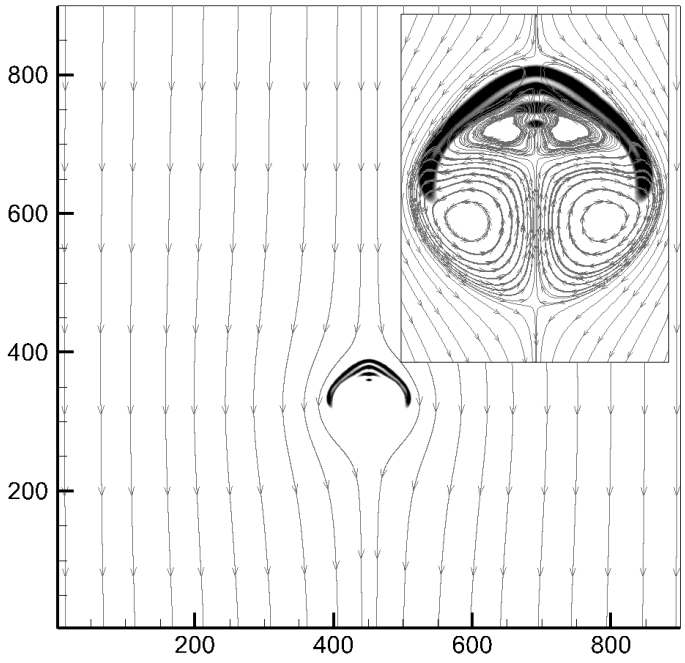

Figure 45. The flow pattern and shape of a bubble rising (case 8, t = 2500).

Two bubble rising under buoyancy

To understand the multiple bubble dynamics – the bubble shape deformation and the bubble coalescence –, we apply the LBM with phase-field modeling to two bubbles in a liquid with buoyancy force.

Two bubbles with radius (R = 20) are located in the domain $5R \times 30R$ vertically. The initial distance between the centers of bubbles is set as $4R$. The no-slip boundary condition is specified on the top and bottom walls of domain, and the side boundaries are assumed to be periodic. The density ratio is set to be 1000 (ρ_H = 1000, ρ_L = 1). The surface tension coefficient and Γ are chosen as 0.5 and 100, respectively. The interfacial layer thickness (W) is taken as 5. The Morton number is set to be 1.

To investigate the influence of the Eötvös number is varied as shown in Table 6.

Table 6. The parameters for the multi bubble rising simulation with large density ratio.

Cases	*Eo*	Gravity magnitude
1	3	9.3843e-07
2	30	9.3843e-06

The simulated bubble movements in the cases 1 and 2 are shown in Figures 46 to 51 and Figures 52 to 59, respectively. From the terminal velocity, the Reynolds numbers of each case are 0.788, and 8.40, respectively.

During the rise of bubble, two signed vortices are created in the wake of the upper bubble. This produces a lower pressure region behind the upper bubble. Therefore, the front portion of the lower bubble becomes narrower and sharper. The head of the lower bubble almost catches up with the bottom of the upper one. In the next moment, the two bubbles merge into a single one. At this time, viscosity and surface tension rapidly smooth out the bridge radius of the bubbles.

Bubble coalescence in case 1 is shown in Figures 46 to 51. Due to the considerable rigidity of the bubbles, the liquid rather quickly becomes squeezed out of the space between the bubbles, and the bubbles merge.

Bubble coalescence in case 2 (Figures 52 to 59) apparently differs from the previous case because of the strong influence of the upper bubble's wake, and the weak secondary vortices appear right under the bubble bottom (Figure 54). When the lower bubble catches up with the upper bubble's wake, it starts to rise much faster and its top becomes narrower. The lower bubble tends to merge with the upper one, but the secondary recirculation under the bottom of the upper bubble precludes an immediate merger. The front of the lower bubble stretches along the bottom of the upper bubble, and, in the next moment, the lower bubble's top merges with the center of the upper bubble's bottom. The recirculating liquid between the bubbles is rapidly squeezed out, and the bubbles form a single, dimpled ellipsoidal bubble.

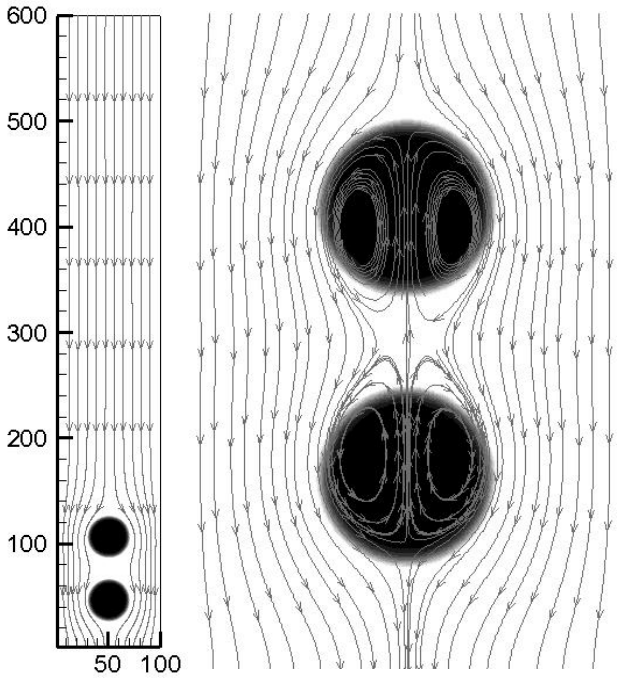

Figure 46. The flow pattern and shape of two rising bubbles (case 1, t = 2000).

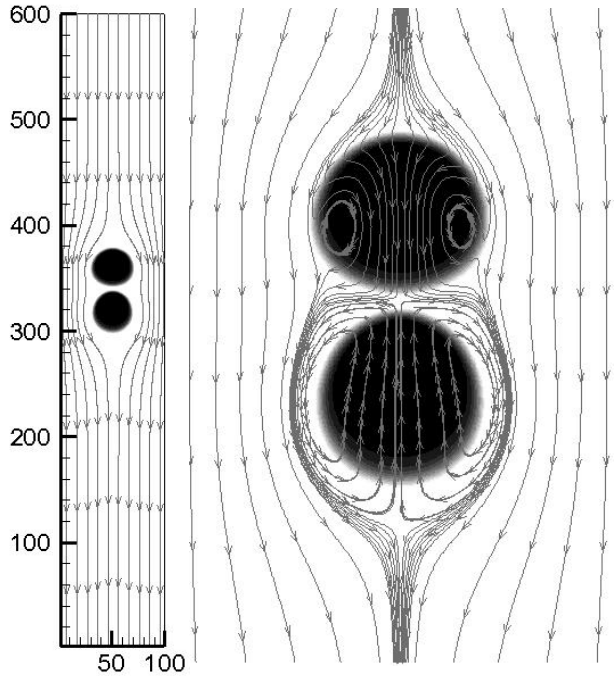

Figure 47. The flow pattern and shape of two rising bubbles (case 1, t = 350000).

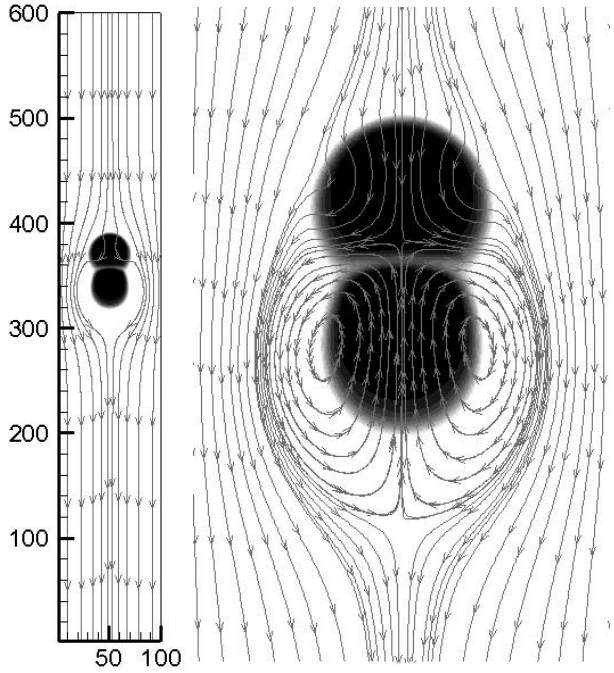

Figure 48. The flow pattern and shape of two rising bubbles (case 1, t = 370000).

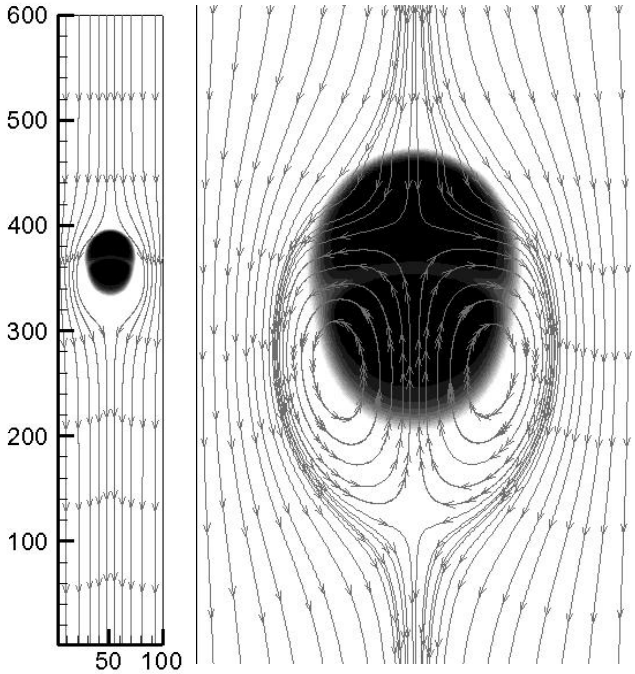

Figure 49. The flow pattern and shape of two rising bubbles (case 1, t = 380000).

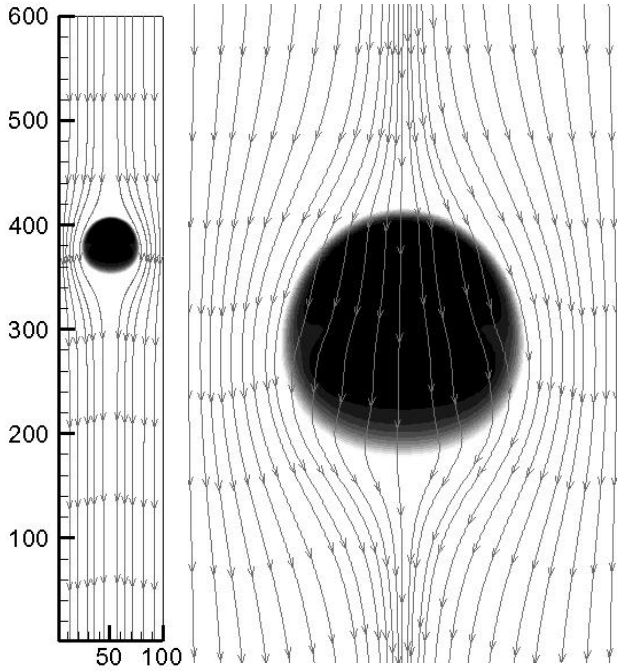

Figure 50. The flow pattern and shape of two rising bubbles (case 1, t = 400000).

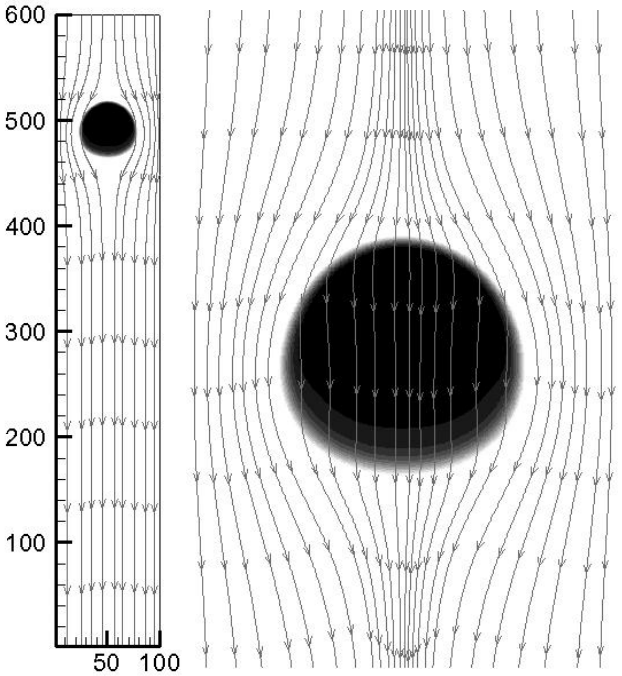

Figure 51. The flow pattern and shape of two rising bubbles (case 1, t = 600000).

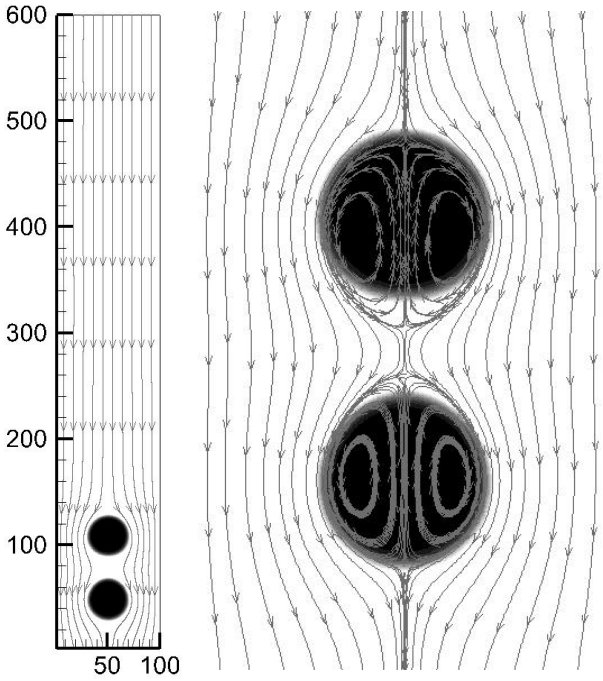

Figure 52. The flow pattern and shape of two rising bubbles (case 2, t = 1000).

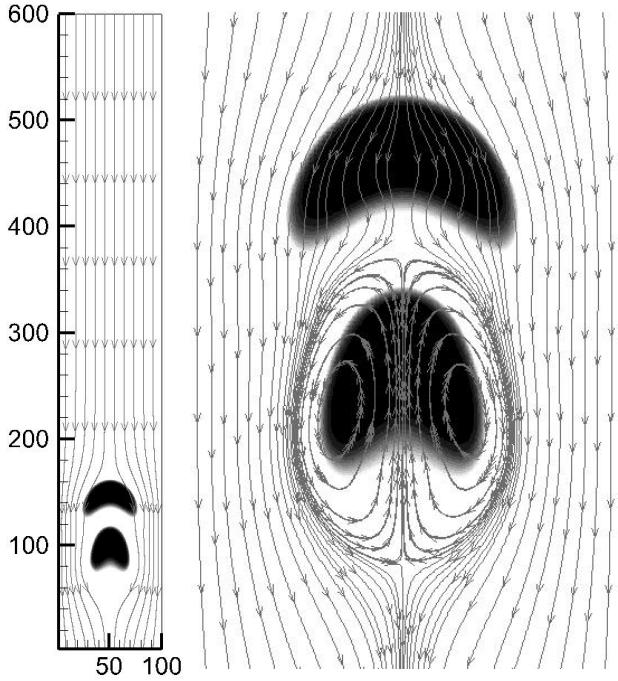

Figure 53. The flow pattern and shape of two rising bubbles (case 2, t = 5000).

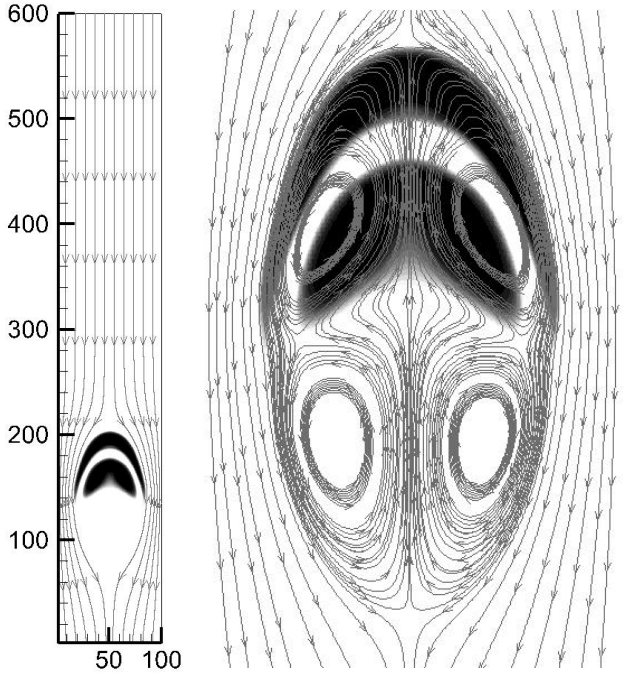

Figure 54. The flow pattern and shape of two rising bubbles (case 2, t = 10000).

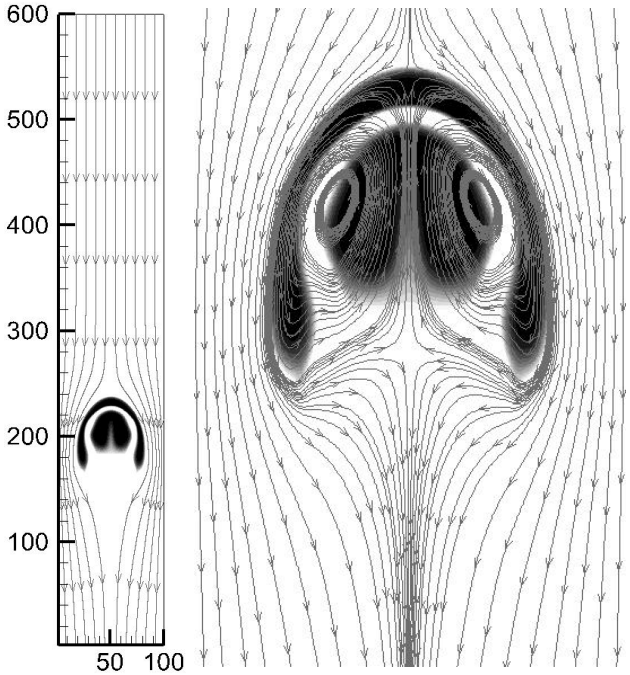

Figure 55. The flow pattern and shape of two rising bubbles (case 2, t = 15000).

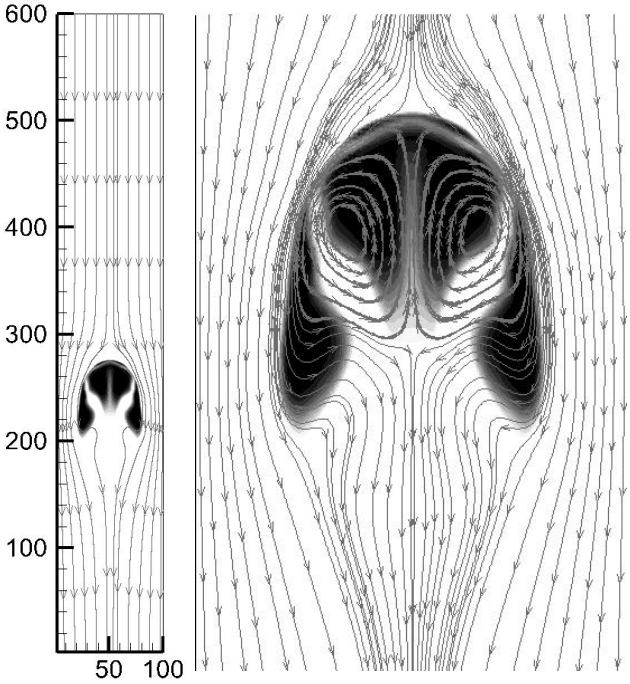

Figure 56. The flow pattern and shape of two rising bubbles (case 2, t = 20000).

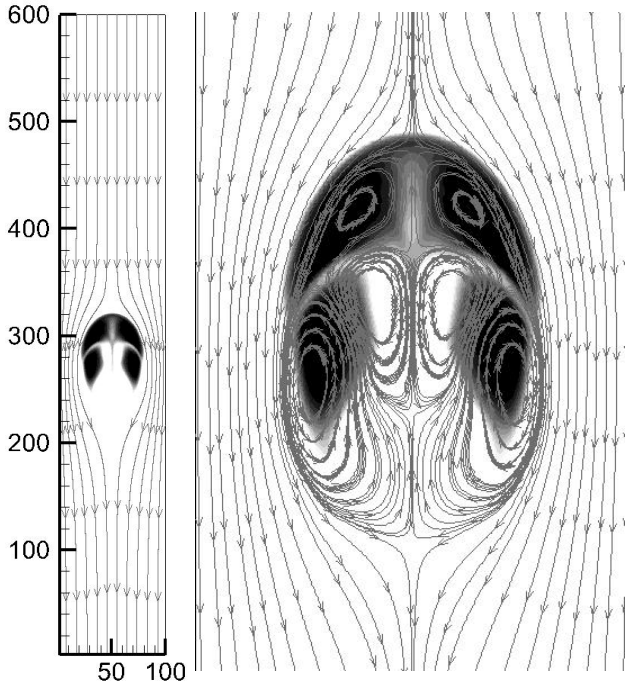

Figure 57. The flow pattern and shape of two rising bubbles (case 2, t = 25000).

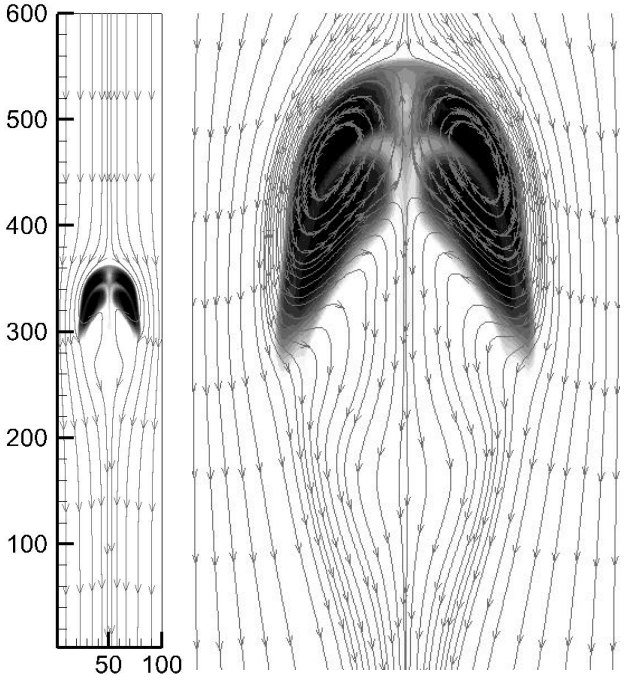

Figure 58. The flow pattern and shape of two rising bubbles (case 2, t = 30000).

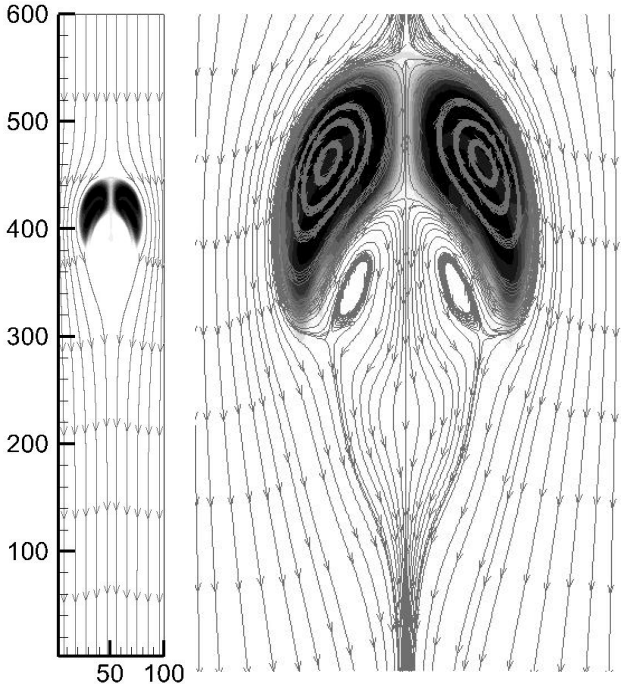

Figure 59. The flow pattern and shape of two rising bubbles (case 2, t = 40000).

CHAPTER IV

CONCLUSIONS

In this thesis, we used a LBM with phase-field modeling to simulate various two-phase problems.

First, the present two-phase modeling method was validated for stationary and moving two-phase interfaces by comparing with theoretical solutions for a single static bubble in a stationary liquid and a capillary wave, respectively. In addition, the capability of the current method to simulate the coalescence of two bubbles and droplets was validated by comparing it with experimental data.

The method was applied to a single and double bubble rising problems. For a single bubble problem, bubble shapes and terminal Reynolds number agreed well with experimental results for different fluid dynamic conditions (Eötvös, and Morton numbers). For the double bubble case, the current method could capture the interaction between bubbles, as well as each bubble dynamics. As a result, the present method can simulate multiphase fluids with large density ratios and the coalescence in the two-dimensional isothermal case.

This method is expected to extend to three-dimension multiphase flow problems by simply adopting the three-dimensional LBM (D3Q19) instead of the D2Q9 LBM. It is also predicted that the adoption of the multiple relaxation time model in the collision step can improve the numerical stability even with small relaxation time; thus,

simulating high Reynolds number multiphase flows. In addition, to simulate convective subcooled boiling, we need to couple thermal models with the present method.

It is hoped that these improvements will lead to a better understanding of various multi-phase interactions and flow patterns. The development of capability to predict convective subcooled boiling heat transfer in the nuclear reactor core will be further pursued.

REFERENCES

1. Hirt CW, Nichols BD. Volume of fluid (VOF) method for the dynamics of free boundaries. *Journal of Computational Physics* 1981; 39:201-225.
2. Unverdi SO, Tryggvason G. A front-tracking method for viscous, incompressible, multi-fluid flows. *Journal of Computational Physics* 1992; 100:25-37.
3. Sethian JA. A fast marching level set method for monotonically advancing fronts. *Proceedings of the National Academy of Sciences of the United States of America* 1996; 93:1591-1595.
4. Cahn JW, Hilliard JE. Free energy of a nonuniform system .1. Interfacial free energy. *Journal of Chemical Physics* 1958; 28:258-267.
5. Bray AJ, Rutenberg AD. Growth laws for phase ordering. *Physical Review E* 1994; 49:R27-R30.
6. Jamet D, Lebaigue O, Coutris N, Delhaye JM. The second gradient method for the direct numerical simulation of liquid-vapor flows with phase change. *Journal of Computational Physics* 2001; 169:624-651.
7. Chen S, Doolen GD. Lattice Boltzmann method for fluid flows. *Annual Review of Fluid Mechanics* 1998; 30:329-364.
8. Yu DZ, Mei RW, Luo LS, Shyy W. Viscous flow computations with the method of lattice Boltzmann equation. *Progress in Aerospace Sciences* 2003; 39:329-367.
9. Gunstensen AK, Rothman DH, Zaleski S, Zanetti G. Lattice Boltzmann model of immiscible fluids. *Physical Review A* 1991; 43:4320-4327.

10. Rothman DH, Keller JM. Immiscible cellular-automaton fluids. *Journal of Statistical Physics* 1988; 52:1119-1127.

11. Ahrenholz B, Tolke J, Lehmann P, Peters A, Kaestner A, *et al*. Prediction of capillary hysteresis in a porous material using lattice-Boltzmann methods and comparison to experimental data and a morphological pore network model. *Advances in Water Resources* 2008; 31:1151-1173.

12. Shan XW, Chen HD. Lattice Boltzmann model for simulating flows with multiple phases and components. *Physical Review E* 1993; 47:1815-1819.

13. Huang HB, Lu XY. Relative permeabilities and coupling effects in steady-state gas-liquid flow in porous media: A lattice Boltzmann study. *Physics of Fluids* 2009; 21:092104.

14. Pan C, Hilpert M, Miller CT. Lattice-Boltzmann simulation of two-phase flow in porous media. *Water Resources Research* 2004; 40:W01501.

15. Li HN, Pan CX, Miller CT. Pore-scale investigation of viscous coupling effects for two-phase flow in porous media. *Physical Review E* 2005; 72:026705.

16. He XY, Chen SY, Zhang RY. A lattice Boltzmann scheme for incompressible multiphase flow and its application in simulation of rayleigh-taylor instability. *Journal of Computational Physics* 1999; 152:642-663.

17. Lee T, Lin CL. A stable discretization of the lattice Boltzmann equation for simulation of incompressible two-phase flows at high density ratio. *Journal of Computational Physics* 2005; 206:16-47.

18. Swift MR, Osborn WR, Yeomans JM. Lattice Boltzmann simulation of nonideal fluids. *Physical Review Letters* 1995; 75:830-833.

19. Orlandini E, Swift MR, Yeomans JM. A lattice Boltzmann model of binary-fluid mixtures. *Europhysics Letters* 1995; 32:463-468.

20. Inamuro T, Ogata T, Tajima S, Konishi N. A lattice Boltzmann method for incompressible two-phase flows with large density differences. *Journal of Computational Physics* 2004; 198:628-644.

21. Zheng HW, Shu C, Chew YT. A lattice Boltzmann model for multiphase flows with large density ratio. *Journal of Computational Physics* 2006; 218:353-371.

22. Jacqmin D. Calculation of two-phase navier-stokes flows using phase-field modeling. *Journal of Computational Physics* 1999; 155:96-127.

23. Kendon VM, Cates ME, Pagonabarraga I, Desplat JC, Bladon P. Inertial effects in three-dimensional spinodal decomposition of a symmetric binary fluid mixture: A lattice Boltzmann study. *Journal of Fluid Mechanics* 2001; 440:147-203.

24. Takada N, Misawa M, Tomiyama A, Hosokawa S. Simulation of bubble motion under gravity by lattice Boltzmann method. *Journal of Nuclear Science and Technology* 2001; 38:330-341.

25. Jamet D, Torres D, Brackbill JU. On the theory and computation of surface tension: The elimination of parasitic currents through energy conservation in the second-gradient method. *Journal of Computational Physics* 2002; 182:262-276.

26. He XY, Zou QS, Luo LS, Dembo M. Analytic solutions of simple flows and analysis of nonslip boundary conditions for the lattice Boltzmann bgk model. *Journal of Statistical Physics* 1997; 87:115-136.

27. Luo LS. Theory of the lattice Boltzmann method: Lattice Boltzmann models for nonideal gases. *Physical Review E* 2000; 62:4982-4996.

28. Huang JJ, Shu C, Chew YT. Mobility-dependent bifurcations in capillarity-driven two-phase fluid systems by using a lattice Boltzmann phase-field model. *International Journal for Numerical Methods in Fluids* 2009; 60:203-225.

29. He XY, Luo LS. A priori derivation of the lattice Boltzmann equation. *Physical Review E* 1997; 55:R6333-R6336.

30. Qian YH, Dhumieres D, Lallemand P. Lattice bgk models for navier-stokes equation. *Europhysics Letters* 1992; 17:479-484.

31. Guo ZL, Zheng CG, Shi BC. Discrete lattice effects on the forcing term in the lattice Boltzmann method. *Physical Review E* 2002; 65:046308.

32. He XY, Doolen GD. Thermodynamic foundations of kinetic theory and lattice Boltzmann models for multiphase flows. *Journal of Statistical Physics* 2002; 107:309-328.

33. Aarts DGAL, Lekkerkerker HNW, Guo H, Wegdam GH, Bonn D. Hydrodynamics of droplet coalescence. *Physical Review Letters* 2005; 95:164503.

34. Chen TL, Chung JN. Coalescence of bubbles in nucleate boiling on microheaters. *International Journal of Heat and Mass Transfer* 2002; 45:2329-2341.

35. Wu MM, Cubaud T, Ho CM. Scaling law in liquid drop coalescence driven by surface tension. *Physics of Fluids* 2004; 16:L51-L54.

36. Harmathy TZ. Velocity of large drops and bubbles in media of infinite or restricted extent. *Aiche Journal* 1960; 6:281-288.

37. Bugg JD, Mack K, Rezkallah KS. A numerical model of taylor bubbles rising through stagnant liquids in vertical tubes. *International Journal of Multiphase Flow* 1998; 24:271-281.

38. Sankaranarayanan K, Shan X, Kevrekidis IG, Sundaresan S. Bubble flow simulations with the lattice Boltzmann method. *Chemical Engineering Science* 1999; 54:4817-4823.

39. Chen L, Garimella SV, Reizes JA, Leonardi E. The development of a bubble rising in a viscous liquid. *Journal of Fluid Mechanics* 1999; 387:61-96.

40. Frank X, Funfschilling D, Midoux N, Li HZ. Bubbles in a viscous liquid: Lattice Boltzmann simulation and experimental validation. *Journal of Fluid Mechanics* 2006; 546:113-122.

41. Kurtoglu IO, Lin CL. Lattice Boltzmann study of bubble dynamics. *Numerical Heat Transfer Part B-Fundamentals* 2006; 50:333-351.

42. Hua J, Lou J. Numerical simulation of bubble rising in viscous liquid. *Journal of Computational Physics* 2007; 222:769-795.

43. Mukundakrishnan K, Quan SP, Eckmann DM, Ayyaswamy PS. Numerical study of wall effects on buoyant gas-bubble rise in a liquid-filled finite cylinder. *Physical Review E* 2007; 76:036308.

44. Li J, Bulusu V, Gupta NR. Buoyancy-driven motion of bubbles in square channels. *Chemical Engineering Science* 2008; 63:3766-3774.

VITA

Donghoon Kim was born in Jeollabuk-do, Republic of Korea. He received a Bachelor of Science degree in computer engineering from The Republic of Korea Naval Academy in 2003. He entered the Department of Nuclear Engineering at Texas A&M University in September 2009. During his graduate studies at Texas A&M University, the author was a graduate research assistant in the Department of Nuclear Engineering under the direction of Professor Yassin A. Hassan. This thesis was written as a requirement for his degree of Master of Science. His email is brandon.kim.navy@gmail.com.

Name:	Donghoon Kim
Address:	Department of Nuclear Engineering, Texas A&M University, 3133 TAMU, College Station, TX 77843-3133
Email Address:	brandon.kim.navy@gmail.com